Surveying shocked molecular hydrogen in the protostellar outflow of BHR71 IRS1 with JWST

Janssen, Adriaan

Surveying shocked molecular hydrogen in the protostellar outflow of BHR71 IRS1 with JWST

THESIS

submitted in partial fulfillment of the
requirements for the degree of

BACHELOR OF SCIENCE
in
ASTRONOMY AND PHYSICS

Author :	Adriaan Janssen
Student ID :	s3340627
Supervisor :	Ewine F. van Dishoeck
Daily supervisors:	Łukasz Tychoniec, Logan Francis, Martijn van Gelder
2^{nd} corrector :	Matthieu Schaller

Leiden, The Netherlands, June 14, 2024

Surveying shocked molecular hydrogen in the protostellar outflow of BHR71 IRS1 with JWST

Adriaan Janssen

Leiden Observatory, Universiteit Leiden
P.O. Box 9500, 2300 RA Leiden, The Netherlands

June 14, 2024

Abstract

As stars often form in clusters, protostellar outflows may be the most important form of feedback in star formation. The James Webb Space Telescope allows for unprecedented detailed examination of the outflows close to protostars. This thesis analysed shocked molecular hydrogen at different locations in the outflow from the Class 0 protostar BHR71 IRS1 obtained using the JWST/MIRI Medium Resolution Spectrograph. We detected 12 rotational transitions and calculated the intensities of each line for comparison with the Kristensen 2023 shock model. Using rotational diagrams, we find that the temperatures in the shocked region are $T_{warm} \sim 1000$K and $T_{hot} \sim 2600$K, which is high compared to the more distant outflow. We also find well-constrained initial conditions using the shock model. Models in agreement with the data report C-type shocks for all locations, except for the aperture closest to the protostar, where the shock is of the CJ-type. C-type shocks have been observed in jet-shocked clouds, which, along with the high temperatures, points to a large influence of the jet in the outflow close to the protostar. The density in the cavity tends to increase towards the protostar but is low in the outer locations compared to previous studies of the environment. Observations agree with the paradigm of more powerful outflows from Class 0 than Class I protostars. 4D grids of the initial conditions were produced that show the minimum distance, which can be used to confine the parameter space of the shock code in order to create a finer grid for shock simulations.

Chapter 1

Chapter 1: Introduction

The formation of most celestial bodies is intrinsically linked to the existence of stars. During their formation process, stars contribute to the creation of planets. Upon reaching the end of their life cycles, some stars undergo supernova explosions, transforming them into white dwarfs, neutron stars, or black holes, and synthesising heavy elements in the process. Life on our planet depends on a star, as it provides light and thus energy. Consequently, the study of stars is a critical area of astrophysical research due to their fundamental role in the universe.

Still, many processes relevant to star formation are not yet understood completely. Star formation is a very inefficient process. Only about $1 - 5\%$ of a cloud's gas mass is converted to stellar mass per free-fall time [1]. This indicates that feedback, the injection of energy, momentum, and mass into the interstellar medium (ISM), some enhanced by turbulence, and magnetic fields, may counteract the star formation [2]. To understand star formation, understanding this feedback and all related processes is important. For the formation of low-mass young stellar objects (YSOs), protostellar outflows may be the most dominant source of feedback as stars often form in clusters[3]. The outflows consist of material ejected from the protostellar system. These outflows create shocks by interacting with the quiescent interstellar medium. Shocks heat the environment, which excites the molecules. The most widely used molecule to trace this emission is CO, which is an important coolant, as it is abundant ($\frac{n(CO)}{n(H_2)} \approx 10^{-4}$) and is easily excited in its low-energy rotational states [4]. An equally important tracer is H_2. Although H_2 does not have a dipole moment due to its symmetry and therefore does not show pure rotational emission at millimetre wavelengths, it does exhibit less frequent quadrupole emission, which is $\sim 137^2$ times less strong [5]. The abundance of hydrogen in the interstellar medium surrounding the protostar ($\sim 90\%$, helium being the other $\sim 10\%$ [6]) makes up for the low probability of emission. The least energetic transition of H_2 requires $\sim 1000K$, so cold H_2 hardly radiates. Only the shocked H_2 has strong emission lines, making it an excellent molecule to trace shocks.

Shocks provide insight into the feedback mechanics of protostars and their environment, leading to a better understanding of the formation of stars. This thesis examines the outflow of a very young, Class 0 protostar BHR71 IRS1 and its molecular hydrogen emission. The data was compared to a shock model by Kristensen et al. (2023)[7], who simulated shocks in a large range of physical environments.

1.1 Star forming regions

In the Milky Way, stars and planets only make up $\sim 3 \cdot 10^{-10}$ of the volume [8], but the space is by no means empty. The main component of galaxies is the interstellar medium (ISM), which consists of all matter and radiation between the stars and other stellar bodies. The ISM of the Milky Way is composed of two physical components. One half of the volume is ionised medium with $n < 0.01\text{cm}^{-3}$ and $T_K > 10^5\text{K}$. The other half is a mixture of warm ionised medium and warm neutral medium with $n \sim 0.1 - 1\text{cm}^{-3}$ and $T_K \sim 10^3\text{K}$ [9]. Due to thermal instabilities, the warm neutral medium is divided into warm neutral media (WNM) and cold neutral media (CNM). This CNM has densities of $n > 10^3\text{cm}^{-3}$ and $T_K < 100\text{K}$ [10]. Most of the mass of the ISM is in the CNM, in the form of clouds. These clouds are highly dynamic and are sites for star formation. The majority of star formation in our galaxy is in Giant Molecular Clouds (GMCs), which can be 50 pc to hundreds of parsecs and can have masses of $10^4 - 10^7\text{M}_\odot$ [11]. However, more nearby formation of stars takes place in smaller clouds, such as the cloud complex ρ Ophiuchi [12] which has a total mass of $550\text{M}_\odot$ [13]. The density and temperature at certain points within the cloud can exceed the Jeans limit, which means that the pressure of the gas outward cannot overcome the gravitational force inwards [14]. As a result, the matter will locally collapse in on itself under the force of gravity. The result is a central dense core, surrounded by an envelope of material. The core becomes optically thick, and pressure and temperature increase. Accretion halts as the core heats until it reaches a temperature where it can dissociate molecular hydrogen. The equilibrium is disturbed and the core collapses further. The resulting object is a protostar [15].

1.2 Protostars

A protostar is a young star that is still gathering mass from its parent cloud. As every system has some angular momentum, the protostar rotates around its axis, accompanied by an accretion disk (rotational can also be induced by the instability of the collapse [17]). Figure 1.1 schematically shows the complete evolution of the protostar, starting from the prestellar core to the planetary system. The main accretion phase is the first phase of the protostar, which is called Class 0. Systems with accretion disks tend to exhibit bipolar molecular outflows [4], due to the infall of material on the rotating protostar in the presence of magnetic fields. These outflows are perpendicular to the accretion disk. Low-mass protostars with envelope and molecular outflow are referred to as young stellar objects (YSOs). In Class 0 protostars, the outflows are powerful and predominantly molecular, mostly CO and SiO. The mass loss rate can be up to $10^{-5} M_\odot\ \text{yr}^{-1}$ [18], which is mostly in the powerful jets. These jets are launched within the smallest angle from the perpendicular of the disk and are traced by low-excitation forbidden transitions of ionic forbidden lines, such as [NeII], [FeII], and [NiII] [19]. Besides the highly collimated jets, there are slower ($< 20\ \text{km s}^{-1}$) molecular outflows at larger angles from the perpendicular. These outflows impact the surrounding envelope and form a bipolar cavity. As the protostar evolves from Class 0 to Class I, the power of the outflow decreases and becomes more atomic, but the primary winds become faster and reach extreme high velocities ($> 50\ \text{km s}^{-1}$). The cavity widens with the angle of the standard high-velocity outflow ($< 50\ \text{km s}^{-1}$). At this stage,

Version of June 14, 2024– Created June 14, 2024 - 14:55

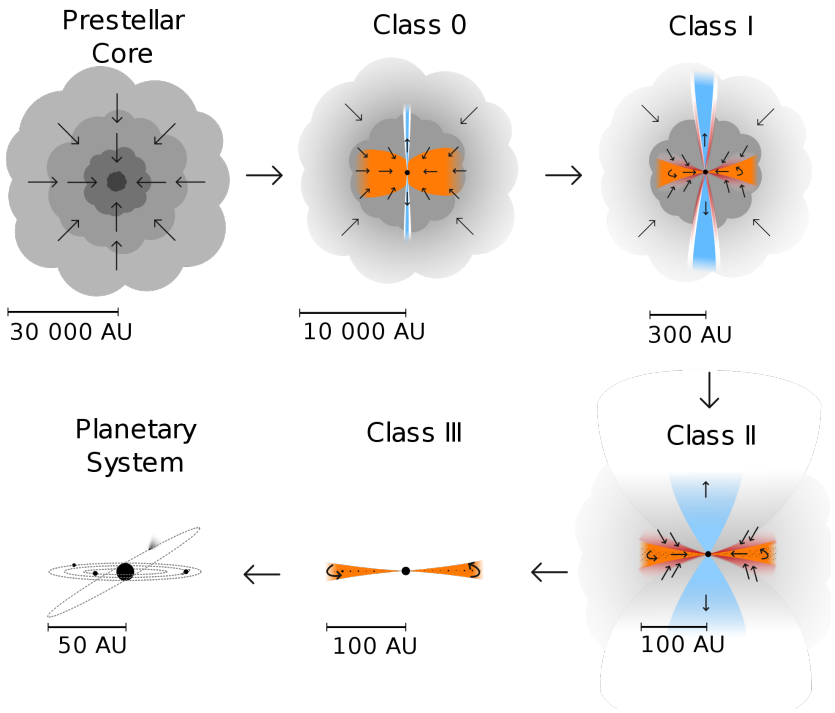

Figure 1.1: *Illustration of protostellar evolution and its different stages. Adapted from Persson (2013) [16]*

most of the envelope mass has already been transferred onto the star and disk. When the envelope fades, the pre-main sequence star and the disk become visible, marking the Class II phase. During the Class II phase, the remaining gas in the disk is trapped in planetesimals or is dispersed by strong stellar winds and radiation [20]. When the envelope is completely absorbed by the star/disk system or photo-evaporated by the increasingly more massive protostar and the disk becomes optically thin due to dissipation, the protostar enters the Class III phase [16]. The evolution of the protostar is often physically marked by the relative masses of the envelope M_{env}, disk M_D and protostar $M_\star$, though these are generally difficult to measure [21]. Another method to determine the difference is by looking at the bolometric temperature associated with the spectral energy densities (SEDs). Class 0 protostars are faint in cold dust emission, while for Class I/II protostars the contributions from the star and disk start to become visible. This is quantifiable using the bolometric temperature, the temperature of a black body with the same frequency. Other methods include (1) the infrared spectral index, given by

$$\alpha_{IR} = \frac{d(\log(\lambda F_\lambda))}{d(\log(\lambda))} \tag{1.1}$$

such that redder protostars correspond to earlier phases [22] and (2) the fraction of the sub-millimetre luminosity and the total luminosity. The infrared spectral index is not useful for Class 0 protostars, as they are too faint and cold in this regime. Table 1.1 provides a summary of the properties.

Table 1.1: *Observational properties of protostellar phases. Adapted from Tychoniec (2021) [15]*

Class	α_{IR}	L_{submm}/L_{Bol}	$T_{Bol}[K]$
0	-	$\geq 0.5\%$	≤ 70
I	≥ 0.3	< 0.5	$70 - 650$
II	-0.3 - -1.6	-	$650 - 2800$
III	≤ -1.6	-	≥ 2800

1.3 Shocks

Molecular outflows consist of high-velocity material ejected from the protostar. When the velocity exceeds the local sound speed, this results in a magnetohydrodynamical (MHD) shock. Similar to supersonic shocks, MHD shocks cause a quick change in temperature, density, and pressure. Shocks occur within the collimated jet and in the outflow cavity walls. The impact of the shock on ambient material leads to bow-shaped emission regions, so-called bow shocks. As the shock clashes with the ambient material, a reverse shock decelerates and compresses the outflow. Sources may produce jets with a 'head' which is followed by one or more 'internal working surfaces', effectively creating more than one shock, following one another [23]. This happens when there is material in the jet with a higher velocity than the downstream material, but a lower velocity than upstream material. This effect is sometimes described as shock bullets. Protostellar outflows can be described by three-fluid MHD plasmas, which means there are three main fluid components: a neutral fluid made up of atoms and molecules, and a plasma composed of ions and electrons[24]. Within this description, shocks can be categorised into two main classes: C- and J-type shocks.

1.3.1 J- and CJ-type shocks

J-type shocks cause a sudden change in the state parameters of quiescent gas and flow variables of the shock. This occurs mostly in regions with insignificant magnetic fields. Upon impact, there is a discontinuous jump in shock velocity (within one mean free path of scatter for neutral atoms) and the state parameters of the medium. This is schematically shown in Figure 1.2(a). Depending on the shock velocity, J-type shocks can be either non-dissociative for H_2 ($V_S < 30$km s^{-1}), with peak temperatures up to a few $10^4 K$, or dissociative with peak temperatures exceeding $10^5 K$ [25]. The ionised material is coupled to the neutral material. If a small magnetic field is present, a magnetic precursor can extend downstream (towards pre-shock material), and the ionised material will impact the ambient material before the neutral shock wave [26]. Due to the precursor, some energy will be transferred, but there is still a discontinuous sub-shock from the neutral flow. This combination of a small precursor and a discontinuous subshock is called a CJ-type shock, shown in Figure 1.2(b).

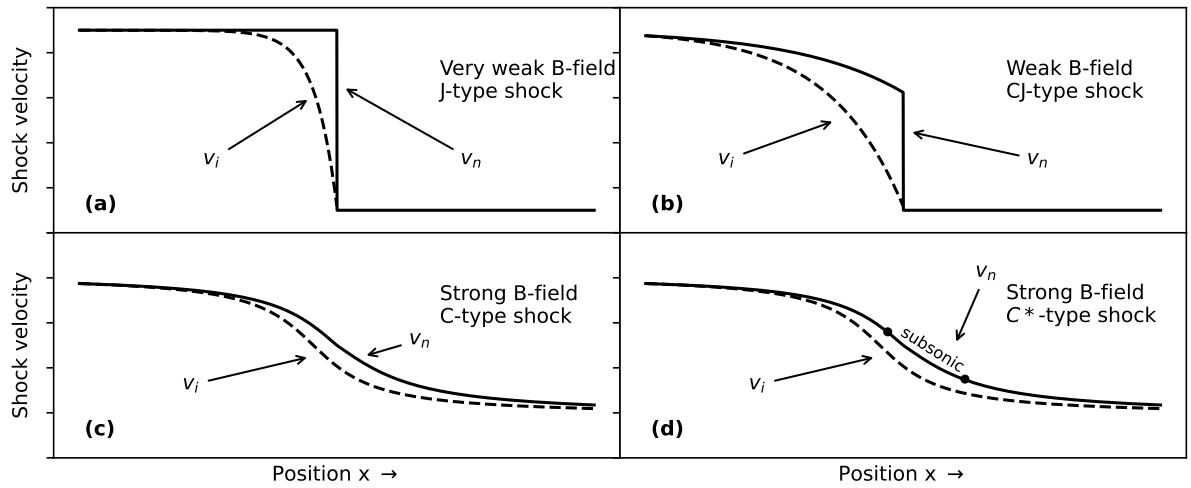

Figure 1.2: *The four shock types. (a) shows the J-type shock, a shock that changes state parameters instantly. (b) displays the CJ-type shock, which has a small magnetic precursor and a discontinuous sub-shock. (c) shows a C-type shock, a shock that has a continuous transition of the flow variables. (d) shows the C^*-type, which is a C-shock that momentarily goes subsonic. The graphics are based on illustrational figures from Draine (1980) [26].*

1.3.2 C- and C*-type shocks

C-type shocks occur when the magnetic field is strong enough that there is no discontinuous sub-shock, but the whole transition of flow variables is continuous. The C-type shock usually only reaches a few thousand Kelvin, which cannot dissociate the H_2. This is why it is also sometimes called a non-dissociative shock. The C-type shock requires the neutral flow to remain supersonic. If the magnetic field is strong enough this can be accomplished, or if the magnetic field is insufficient, radiative cooling can keep the fluid sufficiently cool to remain supersonic. The C-shock is shown in Figure 1.2(c). An extra class of shocks was discovered after the derivation for the C- and J-type shocks. The C* shock was first described by Roberge and Draine [27]. It is a C-type shock that has a supersonic-to-subsonic transition and a subsonic-to-supersonic transition within the downstream flow. This happens when the neutral flow heats up by ion-neutral friction sufficiently so that it goes subsonic [28]. Radiative cooling cools the flow down and the material will return to supersonic speeds. Shocks with this transition are C^*-type shocks, shown in Figure1.2(d).

1.4 Molecular hydrogen emission

Molecular hydrogen, H_2, is a diatomic molecule. It is the most abundant molecule in the ISM, containing about 90% of the mass[6]. Diatomic molecules have hyperfine splitting due to the addition of angular momentum and vibrational momentum to the Hamiltonian of the system, which results in vibrational (ν) and rotational (J) energy levels, governed by selection rules. Non-symmetric diatomic molecules have a dipole moment, which allows for transitions between neighbouring rotational states and between vibrational states: $\Delta\nu = \pm1(\pm2, \pm3, etc)$ with $\Delta J = 0, \pm1$, except for $\Delta\nu = \pm1, \Delta J = 0$. These rules lead to an extensive spectrum for molecules such as CO, which is why they are used so much for observations of shocks.

Symmetric diatomic molecules, such as H_2, do not have a permanent dipole moment, and $\Delta J = \pm 1$ transitions are prohibited. However, hydrogen molecules do have a quadrupole moment, which leads to an extra fine splitting of the energy levels. As a result, rotational-vibrational (rovibrational) transitions of molecular hydrogen can be observed for $\Delta\nu = \pm 1(\pm 2, etc), \Delta J = 0, \pm 2$, except $\Delta\nu = \pm 1, \Delta J = 0$ again. These transitions are less frequent by a factor of α^2 (the fine structure constant), but due to the high abundance of molecular hydrogen, they are still detected[29]. There are three rotational branches, S ($\Delta J = 2$), Q ($\Delta J = 0$), and O ($\Delta J = -2$). The S-branch is emission for pure rotational lines. Notation for the molecular hydrogen transitions is $\nu_u - \nu_l\ S(J_l)$, where u stands for upper and l for lower. The S stands for the S-branch. For example, the line from ν = 0 to $\nu = 0$ and from J = 3 to J = 1 is the 0-0 S(1) line.

1.5 BHR 71

BHR71 (Figure 1.3) is a Bok globule, which is a relatively small and dense cloud of cold gas. Early observations point to a distance of 200 pc from Earth near the southern part of the Coalsack Nebula [30], however, we adopt the distance from more recent studies that suggest 150 pc [31, 32]. BHR71 hosts two protostars: IRS1 and IRS2. IRS1 dominates the luminosity with L= 13.5$L_\odot$ [33], while IRS2 has a luminosity of 1.7$L_\odot$ [34]. IRS1, the target of this thesis, is a Class 0 protostar based on (1) the bolometric temperature, which is estimated at 47K [35], and (2) the fraction of its emission in submillimetre wavelengths [33, 35]. It has an estimated infall radius of 3500 AU and a mass accretion rate of $3 \cdot 10^{-5} M_\odot yr^{-1}$ [36]. The inclination is $\sim 84^\circ$ and the southern lobe is predominantly blue shifted [37]. The coordinates of IRS1 are $12^h01^m36^s.516$ R.A. and $-65^\circ08'49''.298$ Dec [38]. Recently, the Atacama Large Millimeter/Submillimeter Array (ALMA) has shown that the outflows of IRS1 and IRS2 are colliding, south of both objects [39]. This outflow does not affect any observations, as it is outside our field of view.

1.6 The JWST for in-depth examination of outflows

The James Webb Space Telescope (JWST) launch has opened many new observational possibilities for astrophysicists. One of the instruments on board is the Mid InfraRed Instrument (MIRI). This instrument has four operating modes, including the Medium-Resolution Spectrometer (MRS). MRS is an integral-field spectrometer (IFS) that obtains spatially resolved spectroscopic data between 4.9 and 27.9 using integral-field units (IFU) μm [40]. The integral-field units (IFU) split the FOV into spacial slices and each slice is dispersed. The dispersed light hits the detectors. All dispersed slices are recombined to form an image with spatial and spectral information. Previous instruments used for similar measurements, integral field spectroscopy, included the Infrared Space Observatory (ISO) and the Spitzer Space Telescope. Depending on the channel, the JWST MIRI MRS has 1.75 to 900 times the spectral resolution compared to similar instruments in the corresponding wavelength ranges [41]. More importantly, it has a much smaller field of view (FOV) and better spatial resolution. The ISO only provides spectral data for a FOV of at least 14″×20″ [42]. Spitzer has a pixel size of 1.8 arcseconds for the 5.2-26 μm range for a slit of 5.6″×57″ [43], whereas the JWST MIRI MRS instrument has a pixel size of 0.196-0.273 arcseconds for the 4.9-27.9 μm

Version of June 14, 2024– Created June 14, 2024 - 14:55

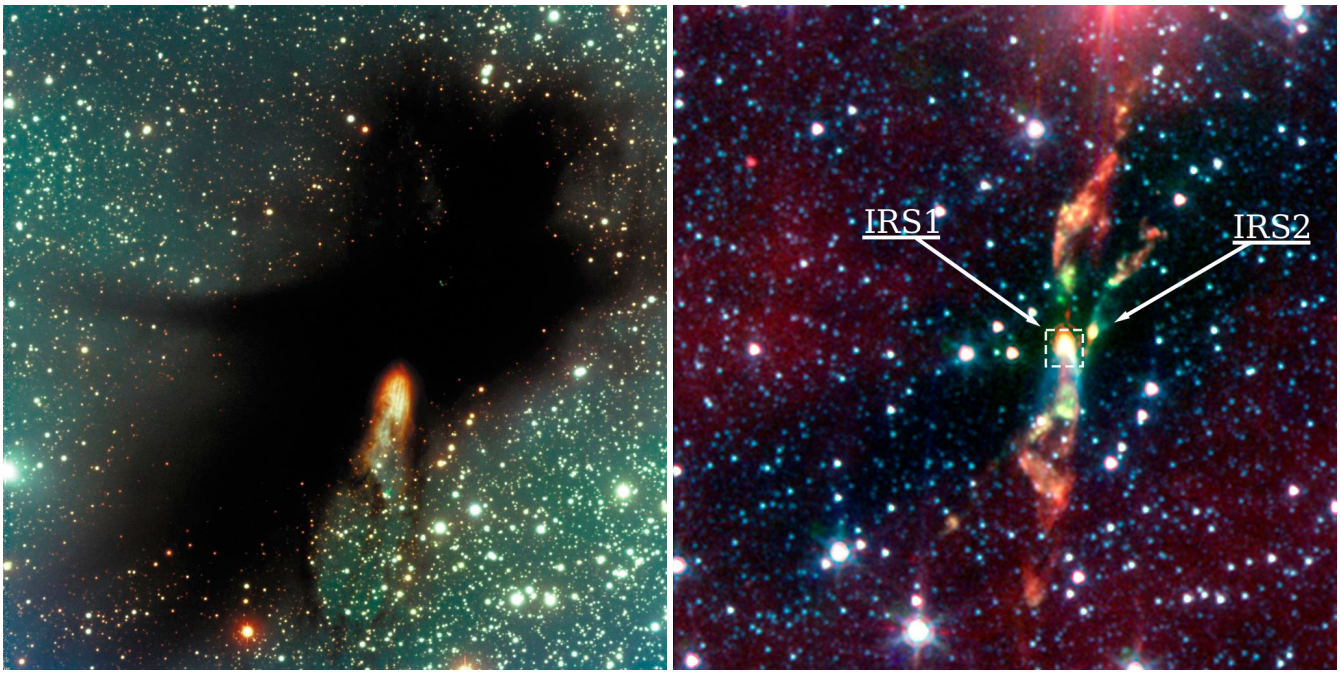

Figure 1.3: *Left panel: BHR71, the prominent black cloud, captured by the Very Large Telescope (VLT) on January 27th, 2003. The yellow jet in the centre is one of the molecular outflows of IRS1. The other outflow is embedded in the cloud. IRS2, located northeast of IRS1, is not visible in this image. Credit and Copyright: J. Alves (ESO), E. Tolstoy (Groningen), R. Fosbury (ST-ECF), R. Hook (ST-ECF), VLT. Right panel: BHR71 in false colours as captured by the Spitzer Space Telescope in infrared. The cloud is transparent in this regime, revealing the northern outflow and IRS2 as a small yellow dot eastern of IRS1. Both protostellar systems are indicated with arrows. The dotted box shows the FOV of the James Webb Space Telescope observation. Credit: NASA/JPL-Caltech/T. Bourke (Harvard-Smithsonian CfA) c2d Legacy Team*

range within a FOV of at most 6.6″×7.7″ [40]. This enables spectral analysis of specific regions within the outflow rather than the entire outflow at closer distances to the protostar. This increased spectral and spatial resolution has opened the door for close examination of shocks in the outflow close to the protostar. Observations can be used to answer questions about the environment of protostellar systems: What are typical values for the density and magnetic field? How do these properties within the outflow change with position? What is the influence of the jet on the shocks? This thesis aims to get closer to an answer to these questions by examining the BHR71 IRS1 outflow close to the protostar. Chapter One provides the background information needed for the thesis. Chapter Two describes the methods used for the results presented in Chapter Three. Lastly, Chapter Four discusses the results and Chapter Five presents the conclusions.

Chapter 2

Methods

2.1 Data from JWST MIRI

The data used for this thesis are from the JWST Observations of Young protoStars (JOYS) Cycle 1 guarantee time observations (GTO) program 1290 (PIs: E. van Dishoeck, H. Beuther). This program was a general survey of protostars, among which was BHR71 IRS1. The observation of BHR71 IRS1 was conducted using the MIRI-MRS instrument, described in the introduction, Section 1.6. MIRI-MRS has four IFU (channels 1 through 4), each divided into three gratings settings (bands): long, medium and short. In one observation, every channel observes using the same band. Therefore, three observations are needed to cover the full wavelength range of 4.9-27.9μm. The estimated uncertainty for the absolute accuracy of the spectro-photometric calibration is $5.6 \pm 0.7\%$ [40]. The FOV, pixel size, wavelength range and resolving power of the bands are given in Table 2.1. The observations of BHR 71 in this work were taken in a 3×3 mosaic, i.e. with 9 different pointings, to cover a larger part of the blue-shifted outflow. Each observation utilised one band and had an exposure time of 200 seconds, resulting in 600 seconds per exposure for the full bandwidth. The resulting file with both spatial and spectral information is called a datacube. These datacubes can be analysed using specialised software. For this project, Carta[1] was the software used to navigate the datacubes.

2.2 Analysis

The analysis aimed to compare observed intensities with intensities calculated using a shock model from Kristensen (2023) for different locations of the protostellar outflow of BHR71 IRS1. First, Section 2.2.1 of the analysis describes the extraction of the spectra. Then, Section 2.2.2 explains the methods used for the calculation of the intensities from the flux. The intensities needed to be corrected for extinction due to the silicate and ice features in the star [44], for which rotational diagrams are needed. Rotational diagrams put the intensities into a physical context. They are tools used to compute the column density and temperatures given a measured set of intensities. This is further described in Section 2.2.4. The method for extinction correction is then described

[1] cartavis.org

Table 2.1: *Relevant MRS spatial and spectral features for each channel and band. FOV is the field of view of the spectral band. Table adapted from Argyriou et al. (2023) [40]*

Spectral band	FOV (″)	Pixel size (″)	λ range (μm)	Resolving power
1 short	3.2 x 3.7	0.196	4.9-5.74	3.320-3.710
1 medium	3.2 x 3.7	0.196	5.66-6.63	3.190-3.750
1 long	3.2 x 3.7	0.196	6.53-7.65	3.100-3.610
2 short	4.0 x 4.8	0.196	7.51-8.77	2.990-3.110
2 medium	4.0 x 4.8	0.196	8.67-10.13	2.750-3.170
2 long	4.0 x 4.8	0.196	10.02-11.70	2.860-3.300
3 short	5.2 x 6.2	0.245	11.55-13.47	2.530-2.880
3 medium	5.2 x 6.2	0.245	13.34-15.57	1.790-2.640
3 long	5.2 x 6.2	0.245	15.41-17.98	1.980-2.790
4 short	6.6 x 7.7	0.273	17.70-20.95	1.460-1.930
4 medium	6.6 x 7.7	0.273	20.69-24.48	1.680-1.770
4 long	6.6 x 7.7	0.273	24.19-27.9	1.630-1.330

in Section 2.2.5. Finally, Section 2.3 describes the shock model, its output, and the methods used for the comparison with the observation.

2.2.1 Extraction of the spectra

In Carta, circular apertures were drawn at certain locations of the outflow. The exact coordinates of the centres are reported in Table 2.2. They have an aperture radius of 0.65 arcseconds. The apertures are chosen arbitrarily, slightly based on the molecular hydrogen brightness and location along the flow. The left image of Figure 2.1 illustrates the locations of the aperture extractions and the source, marked by white circles and a star symbol, respectively. The right image of Figure 2.1 also has a [Ni II] emission line contour overlay. This line indicates the approximate location of the inner jet.

Table 2.2: *Coordinates of the locations of the apertures on the protostellar outflow.*

Aperture	R.A.	Dec
A	$12^h01^m36^s.553$	-65°08′50″.908
B	$12^h01^m36^s.650$	-65°08′53″.015
C	$12^h01^m36^s.395$	-65°08′52″.765
D	$12^h01^m36^s.593$	-65°08′54″.764
E	$12^h01^m36^s.497$	-65°08′56″.264
F	$12^h01^m36^s.287$	-65°08′55″.371

Version of June 14, 2024– Created June 14, 2024 - 14:55

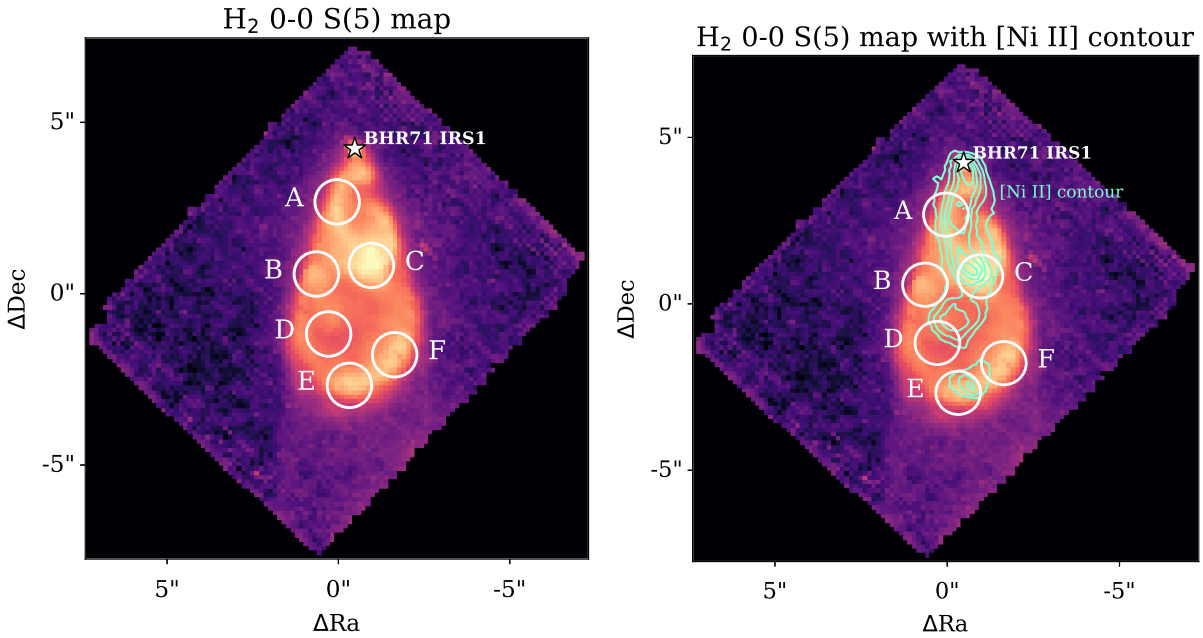

Figure 2.1: *The apertures from which spectra are extracted. The plot is an integrated intensity map of the H_2 0-0 S5 line, shown on the log scale. The left image shows only the emission line and the right image shows an overlay of the contours of Ni II $2D\frac{5}{2} - 2D\frac{3}{2}$. The contours range from 40% to 90% of the maximum flux, in steps of 10% The metal line traces the path of the inner high-velocity jet. The location of the protostar in this image is based on the location with the highest continuum flux.*

Apertures are useful because the different channels of the MIRI MRS have varying resolving powers. Spectra from pixels within the apertures are summed. At the edges of the apertures, only the fraction of each pixel within the aperture is included. This approach solves the issue of varying pixel sizes and simplifies the calculation of the intensity from the flux using the solid angle. Additionally, it enhances the signal-to-noise ratio (S/N) and solves the problem of undersampled channels at the lower wavelengths. Carta is only used to visualise the locations and to export the coordinates to a text file. Extraction for the data was done in Python following the procedure of van Gelder et al.(2024)[45]. The Python script sums the spectra within the apertures. It takes care of residual fringe on the spectrum level that was not yet removed by the calibration pipeline and creates stitched spectra that are exported to data files. Molecular hydrogen emission was detected in all resulting spectra, as well as several molecular and ion lines (e.g. CO, [Ni II], [Fe II]). The MIRI range H_2 lines are listed in Table 2.3. These lines were identified using the line list of Tychoniec (2024) [46]. Not all emission lines were detected in the spectra, and 1-1 S(8) overlaps with a [Fe II] line. Two spectra are shown in Figure 2.2, in which the identified emission lines are marked. From the spectra, the line intensities were calculated.

2.2.2 Calculation of the intensity of spectral lines

Three steps were taken to obtain the intensities of the emission lines, which are needed for the rotational diagrams. The first step was to remove the CO-lines. The second was removing the continuum around the lines and calculating the uncertainty on the

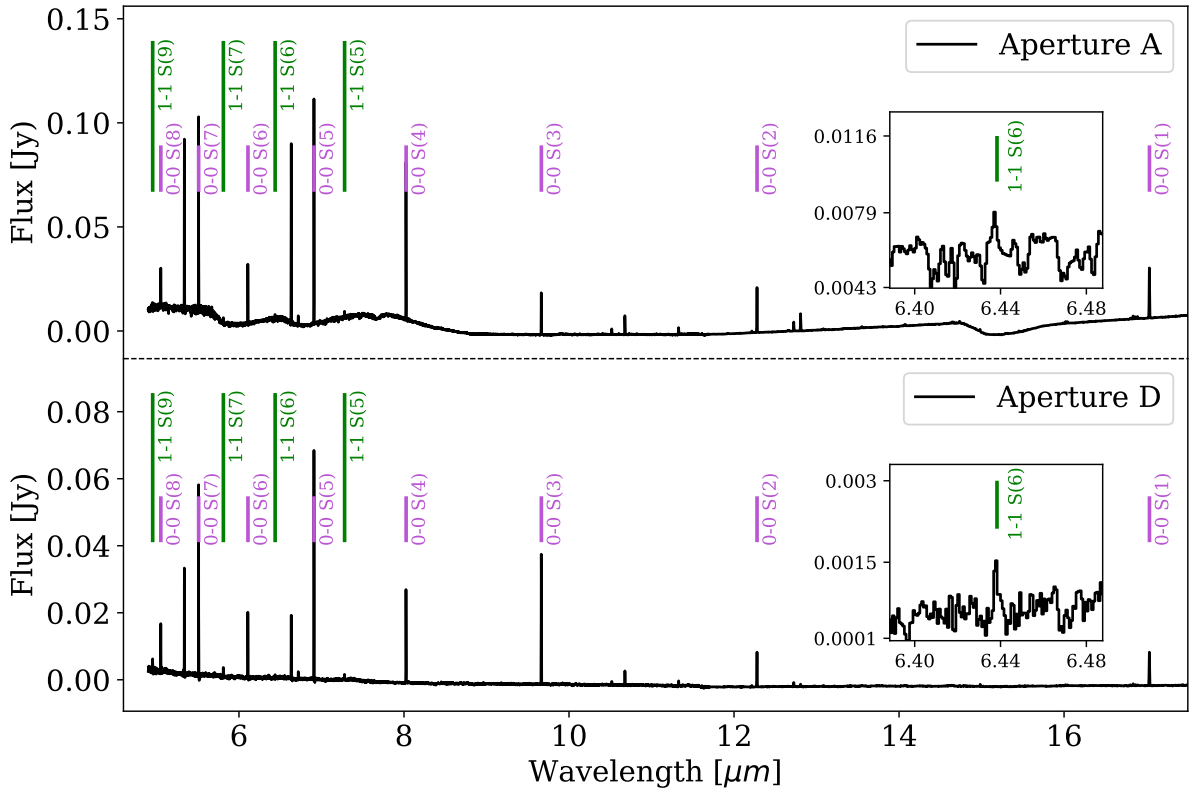

Figure 2.2: *MIRI-MRS spectra from two apertures. The relevant H_2 rotational quadrupole emission lines are marked. The longer green markers indicate $v = 1 - 1$ transitions, while the shorter purple markers indicate $v = 0 - 0$. The insets show the 1-1 S6 lines, as they are faint transitions. The axes have the same units as the axes of the main figure. Top: Spectrum of aperture A, close to the protostar. Bottom: Sprectrum of aperture D, further away from the protostar.*

flux. The third step was to fit the Gaussian and calculate the integral. The whole procedure is shown in Figure 2.3. Except for the CO-line fit, the fitting was done using the Python SciPy 1.13.1 [47] *curve_fit* package, which uses an iterative nonlinear least squares algorithm, the Trust Region Reflective algorithm [48].

Removing CO-lines

CO is an asymmetrical molecule with strong IR emission and is abundant in the ISM [4]. The end of the CO spectrum overlaps with 1-1 S(9)/S(7) and 0-0 S(8)/S(7), which increases the flux of the H_2 emission line at the corresponding wavelengths. To remove this feature, we custom-fitted the CO spectrum for every aperture. The fitting was performed using a slab model, following a procedure similar to that described by Tabone et al. (2023) [49]. The molecular data for CO was retrieved from the HITRAN database [50]. The resulting CO lines were subtracted from the spectrum, which corrects the flux of the H_2 lines. The CO fit is done after continuum subtraction, which is why the fit has base 0. This makes no difference for the intensity of the 1-1 S(9) line. The CO-line fit is shown in Figure 2.3a.

Version of June 14, 2024– Created June 14, 2024 - 14:55

Removing the continuum and calculating error mass

To remove the continuum, the spectra were sliced 1000 km s^{-1} around the rest wavelengths of the H_2 lines of interest. The rest wavelengths were taken from Roueff et al. (2019)[51]. Despite slight shifts in frequency between the lab value and the observed lines, velocities are comparable (on average < 60kms^{-1}) to the MRS resolution. Within 1000 km s^{-1}, no other lines interfere with our lines of interest. At this scale, the local continuum can be approximated by a linear function. A Gaussian with a linear base,

$$f(x) = h + mx + ae^{\frac{-(x-\mu)^2}{2\sigma^2}}, \tag{2.1}$$

was fitted to each clipped spectrum, using the SciPy *curve_fit* package. The linear equation ($h + mx$) accounts for the local continuum and was subtracted from all data points. The standard deviation was calculated 5σ outside the Gaussian mean, effectively removing the line. This standard deviation was used as an uncertainty on the flux for the fit of the emission lines with the continuum subtracted.

Final Gaussian fit and intensity calculation

The final fit was done using the standard Gaussian,

$$f(x) = ae^{\frac{-(x-\mu)^2}{2\sigma^2}} \tag{2.2}$$

and returns a, μ and σ. The difference with the continuum fit is that the uncertainty on the flux was propagated using the fitting package, which returns an uncertainty on a, μ and σ. These parameters could be used to calculate the area under the curve using

$$F_\nu = \sqrt{2\pi}a\sigma \cdot 10^{-23}[\text{erg s}^{-1}\text{cm}^{-2}\text{Hz}^{-1}]. \tag{2.3}$$

The uncertainty was obtained using the uncertainties on a and σ from the fit and the operation of error propagation, resulting in the following equation:

$$F_{\nu_{err}} = \sqrt{(\sqrt{2\pi}\sigma a_{err})^2 + (\sqrt{2\pi}a\sigma_{err})^2} \cdot 10^{-23}[\text{erg s}^{-1}\text{cm}^{-2}\text{Hz}^{-1}]. \tag{2.4}$$

The factor 10^{-23} is the conversion from Jy to erg s^{-1} cm^{-2} Hz^{-1}. The whole process is shown for the 1-1 S9 transition in Figure 2.3. All fits for every aperture are shown in Appendix A. Using the integrated flux and the aperture radius for the solid angle, the intensity was calculated using

$$I_\nu = \frac{F_\nu}{\Omega_{aper}} = \frac{F_\nu}{\pi(0.65'')^2}. \tag{2.5}$$

2.2.3 Integrated intensity maps

Continuum-subtracted flux maps are useful tools to visualise where the emission is coming from. A clip was created around 250 km s^{-1} of each laboratory value of the transitions, to ensure that the line would be within that range. This is done for every spatial pixel in a data cube. Then the median was calculated around 1000 km s^{-1} of the transitions. This is approximately the continuum noise strength around the emission line. The median was subtracted from the wavelength pixel flux value and all values within the 250 km s^{-1} domain were summed to approximate the integrated flux. This resulted in 12 flux maps, where the continuum is subtracted.

Version of June 14, 2024– Created June 14, 2024 - 14:55

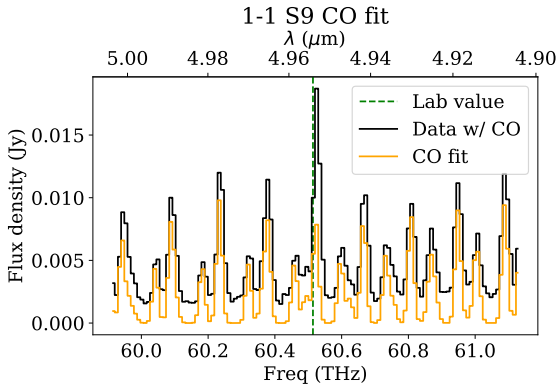

(a) CO line fit (orange line) for aperture E on top of the data (black line), shown for the 1-1 S9 transition.

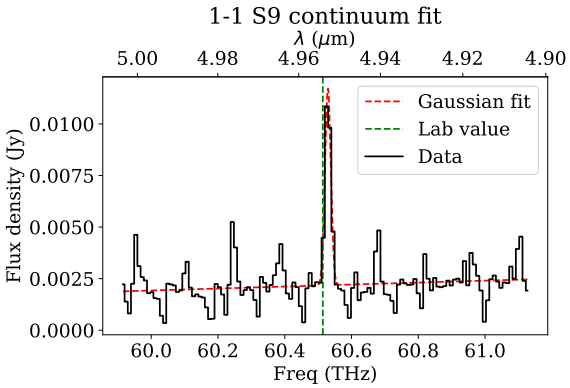

(b) Gaussian with a linear base-fit (dashed red line) to the emission line (black line). The linear base is subtracted from the entire domain.

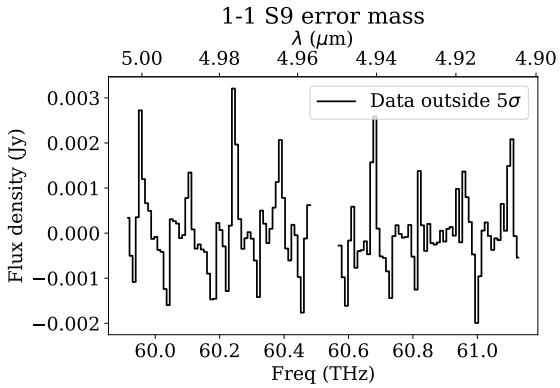

(c) The spectrum within the chosen domain, with the emission line removed. The standard deviation is calculated for the uncertainty on the flux.

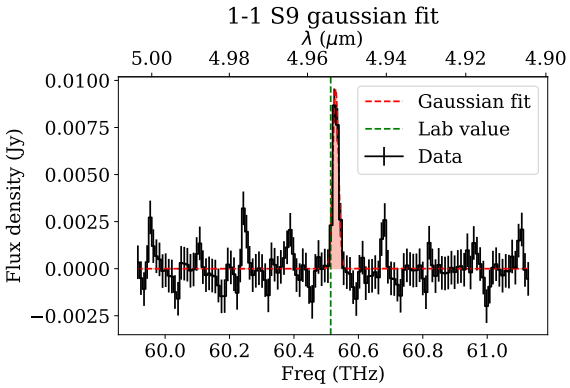

(d) The final Gaussian fit (dashed red line), including the uncertainties on the flux, returns the desired parameters to calculate the area. The area is shaded red.

Figure 2.3: *Procedure for calculating the total flux from the emission lines. The steps are described in the panels, starting at a and ending at d. Note that the wavelength axis high to low, which indicates that the lines are slightly blueshifted.*

2.2.4 Rotational Diagrams

A rotational diagram is a tool for calculating the temperature and total column density when you know the intensities of multiple transitions of one species. The column density is the flattened density of material along the line of sight, in units of cm^{-2}, defined as

$$N = \int n ds. \tag{2.6}$$

The rotational diagrams were created using the relation between the column density of all hydrogen molecules and the column density of hydrogen molecules in an excited state. This is given by the Boltzmann distribution

$$\frac{N_u}{g_u} = \frac{N_{tot}}{Q(T_{rot})} e^{-E_u/kT_{rot}}, \tag{2.7}$$

where N_u is the column density of the upper state, g_u is the degeneracy of the upper (rotational) state, N_{tot} is the column density of all molecules, Q is the partition function, E_u is the energy of the upper state and T_{rot} is the temperature of the medium. If a medium is in local thermal equilibrium (LTE), the excitation temperature equals the temperature of the medium. When we assume an optically thin medium, I_ν is given by

$$I_\nu = \frac{h\nu A_{ul} N_u^{thin}}{4\pi}, \tag{2.8}$$

which states that the intensity is a number of molecules in a column N_u^{thin} that emit photons with probability A_{ul} and energy $h\nu$, divided by the solid angle of a sphere. Rearranging this gives an expression for the column density

$$N_u^{thin} = \frac{4\pi I_\nu}{h\nu A_{ul}}. \tag{2.9}$$

By combining this expression with equation 2.7, we get

$$\frac{4\pi I_\nu}{g_u h\nu A_{ul}} = \frac{N_{tot}}{Q(T_{rot})} e^{-E_u/kT_{rot}} \tag{2.10}$$

Taking the logarithm of both sides results in

$$y = \ln\left(\frac{4\pi I_\nu}{g_u h\nu A_{ul}}\right) = \ln\left(\frac{N_{tot}}{Q(T_{rot})}\right) - \frac{E_u}{kT_{rot}}. \tag{2.11}$$

When defining $x = E_u/k$, this is a linear equation of the form $y = mx + b$ with

$$m = -\frac{1}{T_{rot}} \tag{2.12}$$

and

$$b = \ln\left(\frac{N_{tot}}{Q(T_{rot})}\right). \tag{2.13}$$

The relevant values of the parameters in the equations are given in Table 2.3. The only two unknowns are T_{rot} and N_{tot}, which can be fitted for. This procedure is for a single component of the H_2, while there could be hotter or colder components present. In such a case you can use a modified version of 2.10,

$$y = \ln\left(N_{\text{warm}} \frac{\exp\left(-x/T_{\text{warm}}\right)}{Q\left(T_{\text{warm}}\right)} + N_{\text{hot}} \frac{\exp\left(-x/T_{\text{hot}}\right)}{Q\left(T_{\text{hot}}\right)}\right), \tag{2.14}$$

which results in two-column densities and two temperatures, named warm ($T > 10^2$K) and hot ($T > 10^3$K). This equation assumes two components in the aperture. If you have more data points, more components could be required, but two were sufficient in the case of this thesis. The total column density is $N_{tot} = N_{warm} + N_{hot}$.

Table 2.3: *The rotational transitions in the MIRI-MRS range and relevant properties for the rotational diagrams. E_u is the upper state energy, A_{ul} is the Einstein A coefficient for the transition and g_u is the degeneracy of the upper state. Values retrieved from Roueff et al. 2019[51]*

Transition	λ_{rest}	$E_u(K)$	$A_{ul}(s^{-1})$	g_u
0-0 S(1)	17.035	1015.1	4.76(-10)	21.0
0-0 S(2)	12.279	1681.6	2.754(-9)	9.0
0-0 S(3)	9.6649	2503.7	9.833(-9)	33.0
0-0 S(4)	8.0258	3474.5	2.642(-8)	13.0
0-0 S(5)	6.9091	4586.1	5.877(-8)	45.0
0-0 S(6)	6.1089	5829.8	1.142(-7)	17.0
0-0 S(7)	5.5111	7196.7	2.001(-7)	57.0
0-0 S(8)	5.0528	8677.1	3.235(-7)	21.0
1-1 S(1)$^{(a)}$	17.932	-	-	-
1-1 S(2)$^{(a)}$	12.928	-	-	-
1-1 S(3)$^{(a)}$	10.178	-	-	-
1-1 S(4)$^{(a)}$	8.4530	-	-	-
1-1 S(5)	7.2807	10341.2	5.434(-8)	45.0
1-1 S(6)	6.4383	11521.1	1.047(-7)	17.0
1-1 S(7)	5.8111	12817.2	1.82(-7)	57.0
1-1 S(8)$^{(b)}$	5.3300	-	-	-
1-1 S(9)	4.9533	15721.5	4.373(-7)	69.0

Notes: *The brackets indicate the order of magnitude: $b(a)$ is $b \times 10^a$. $^{(a)}$Not detected in the outflow of BHR71 IRS1. $^{(b)}$Overlaps with [Fe II] line.*

2.2.5 Extinction correction

Apart from extinction due to the diffuse interstellar medium, dense molecular clouds show their own extinction curve [52]. This extinction curve most prominently shows peaks for silicate grains, H_2O ice and methanol ice. The ices reside on the surfaces of silicate grains. The molecules absorb a fraction of the light emitted by the molecular hydrogen. Some lines are more suppressed than others, e.g. 0-0 S(3) is deeply embedded in a silicate feature. An empirical extinction curve for star-forming regions has been created by McClure (2009) [44], which was used to correct the intensities of the transitions. This correction is incorporated into Equation 2.9 with an extinction factor A_λ, which is a correction variable applied to the magnitude. As the magnitude is

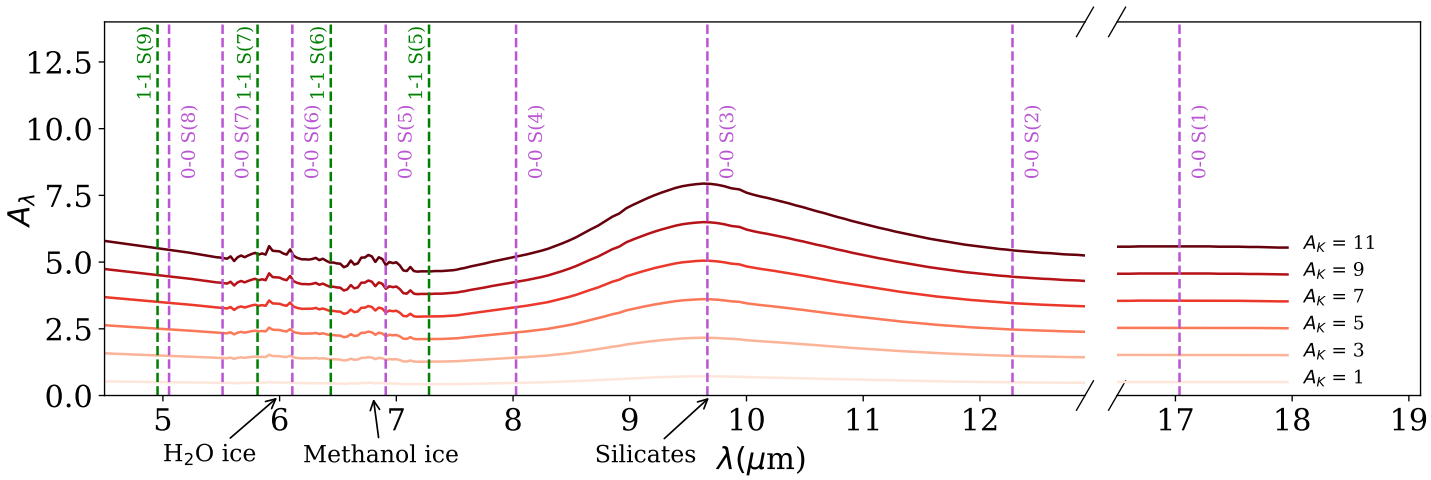

Figure 2.4: *Extinction curve for dense molecular clouds by McClure (2009) for various values of A_K (solid lines). The H_2 transitions are overlaid (dashed lines) in the figure. The main characteristics are the 6.0 μm H_2O, 6.8 μm methanol and the 9.7 μm silicate features.*

logarithmic, the factor is incorporated into the equation as follows:

$$\ln\left(\frac{4\pi I_\nu}{g_u h\nu A_{ul}} * 10^{-2.5A_\lambda}\right) = \ln\left(\frac{N_{tot}}{Q(T_{rot})}\right) - \frac{E_u}{kT_{rot}}. \tag{2.15}$$

McClure provides $\frac{A_\lambda}{A_K}$, which are normalised values for A_λ, using the total extinction A_K. A_K is roughly related to the visual extinction A_V and $0.3 \leq A_K \leq 7$ is approximately equivalent to $3 \leq A_V \leq 50$[1][44]. The extinction was determined by fitting a single temperature component to 0-0 S(1) through S(4) and varying A_K. This linearises the first four line intensities, as we expect these transitions to be roughly in a straight line. Each aperture was fitted for separately, as the extinctions differ at different locations. Two examples are shown in Figure 2.5.

2.3 Shock model for JWST observations

The thesis mainly aimed to compare the observed emission line intensities with the Kristensen et al. (2023, hereafter K23) shock models. The model is based on the Paris-Durham shock model, a stationary, plane-parallel, multifluid shock wave simulation. This shock model, first published in 1985 [53], has undergone many improvements, but the version used by K23 is described in Godard et al. (2019) [54]. Although the model is publicly available on the ISM platform[2], this thesis only used the results from K23. The shock model simulates a 6D parameters space with initial conditions for the pre-shock density ($n_H = n(H) + 2n(H_2)$), the shock velocity (v_s), the strength of the transverse magnetic field (b[3]), the external UV radiation (G_0 in units of the field from Mathis et al. 1983[55]), the cosmic-ray ionisation rate of H_2 (ζ_{H_2}) and the fractional polycyclic aromatic hydrocarbon (PAH) abundance ($X(PAH)$). It then returns a set of final conditions, including line intensities of the rotational H_2 transitions. The first

[1] $\frac{A_V}{A_K} = 7.75$ provided that $R_V = 5$.
[2] http://ism.obspm.fr/shock.html
[3] A scaling factor for the transverse magnetic field strength $B = b \times \sqrt{n_H(cm^{-3})}\mu G$

Version of June 14, 2024– Created June 14, 2024 - 14:55

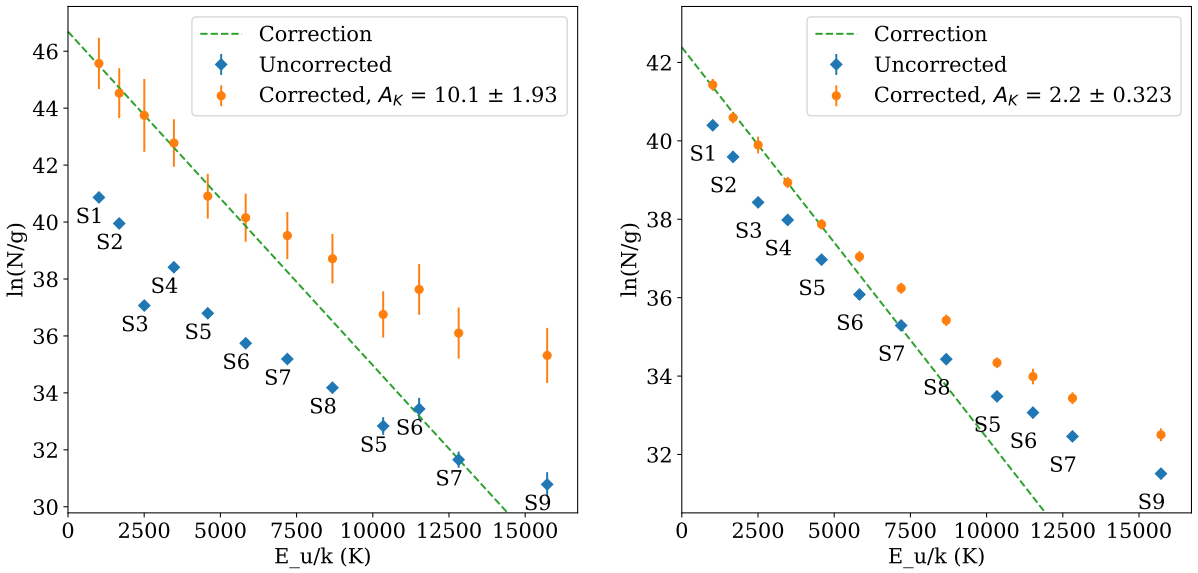

Figure 2.5: *Two examples of linearisation for rotational diagrams using the extinction curve. The left figure is aperture A, and the right is aperture E. The blue diamonds are the uncorrected data points and the orange dots are the corrected points. The increased error bars are from the extinction correction uncertainty. The dashed green line is the best linear fit through the 0-0 S(1)-(4) transitions. The calculated A_K are* 10.1 ± 1.93 *for aperture A and* 2.2 ± 0.32 *for aperture E.*

four parameters, n_H, v_s, b, and G_0 are of particular importance, as they impact the intensities significantly, following from the MHD equations [26]. The PAH abundance, X(PAH), is important as it shields the H_2 from UV radiation, effectively decreasing the intensity [56]. The cosmic ray ionisation rate, ζ_{H_2}, is similar to G_0, as the externally ionise H_2, increasing the intensities of the transitions. K23 summarised the impact of each initial condition. v_s and b together set the shock type. v_s and n_H set the kinetic energy E_{kin}. G_0 has little effect on J-type shocks but changes the excitation for C-type shocks with $E_{UV} > E_{kin}$. ζ_{H_2} is mainly important when G_0 is 0, otherwise it has no significant impact. Table 2.4 shows the initial conditions grid. Some combinations of parameters were not simulated, as they either do not produce a shock (high b and low v_s) or result in self-irradiated shocks, which are not treated in this version of the shock model (v_s >30km s^{-1} for $b < 3$). There are a few other limitations of the model, summarised in Appendix C.

The format of the output used for the comparison is shown in Table 2.5, which is a tabular form of the data files provided by the paper. The final parameters space is extensive, but we only looked at the molecular hydrogen column density (N(H_2)), the maximum temperature of the shock ($T_{gas,max}$), the ortho-to-para ratio (OPR), the shock width (Delta-z in AU), and the intensities for the relevant molecular hydrogen lines. Using this output, we aimed to constrain the initial conditions of the shocks in the outflow of BHR71 IRS1.

Table 2.4: *Shock grid parameters that were simulated, adapted from K23.*

Parameter	Values
$n_H{}^{(a)}$ $\left(\mathrm{cm}^{-3}\right)$	$10^2, 10^3, 10^4, 10^5, 10^6, 10^7, 10^8$
$\mathrm{b}^{(b)}$	0.1, 0.3, 1.0, 3.0, 10.0
v_s $\left(\mathrm{km\,s}^{-1}\right)$, $b = 0.1, 0.3, 1.0$	2, 3, 4, 5, 10, 15, 20, 25, 30
$v_s\left(\mathrm{km\,s}^{-1}\right)$, $b = 3.0$	10, 20, 30, 40, 50, 60
v_s $\left(\mathrm{km\,s}^{-1}\right)$, $b = 10.0$	20, 40, 60, 80, 90
$\mathrm{G}_0^{(c)}$	$0, 10^{-1}, 10^0, 10^1, 10^2, 10^3$
$\zeta_{\mathrm{H}_2}^{(d)}$ $\left(\mathrm{s}^{-1}\right)$	$10^{-17}, 10^{-16}, 10^{-15}$
X(PAH)	$10^{-8}, 10^{-7}, 10^{-6}$

Notes: *$^{(a)}$Proton density $n_H = n(H) + 2n(H_2)$. $^{(b)}$b is a scaling factor for the transverse magnetic field, $B = b \times \sqrt{n_H(cm^{-3})}\mu G$. $^{(c)}G_0$ in units of the field from Mathis et al. 1983. $^{(d)}H_2$ cosmic-ray ionisation rate*

Table 2.5: *Physical parameters simulated by the K23 shock model, sub-selection of data published. This is an example of what a table looks like. For actual tables/data, we refer to the original paper and the data product.*

n_H $\left(\mathrm{cm}^{-3}\right)$	v_s $\left(\mathrm{kms}^{-1}\right)$	b	G_0	ζ_{H_2} $\left(\mathrm{s}^{-1}\right)$	X(PAH)	Type $^{(a)}$	Quantity X	$\cdots$
10^2	3.0	0.1	0	10^{-17}	10^{-06}	0	Example	$\cdots$
10^2	3.0	0.3	0	10^{-17}	10^{-06}	1	Example	$\cdots$
10^2	3.0	1.0	0	10^{-17}	10^{-06}	1	Example	$\cdots$
$\ldots$	$\ldots$	$\ldots$	$\ldots$	$\ldots$	$\ldots$	$\ldots$	$\ldots$	$\ldots$

Notes: *$^{(a)}$Types are provided as a number, i.e. 0 is J-type, 1 is for C-type, 2 is for C*-type and 3 is for CJ-type. Models that did not converge have 99 as Type output.*

2.3.1 Method for the comparison to the model

One of the Tables from the K23 paper provides intensities of rovibrational molecular hydrogen lines, calculated by simulating the model with a combination of the six input parameters. The calculated H_2 lines include the lines that were observed. To compare the intensities from the model and the observed intensities, the observed intensities were corrected for extinction using the A_K value found using the extinction correction on the rotational diagrams. To find the best model, a similar method was used as in Villa Vélez et al. (2024) [57]. Their method relies on a distance between the model and

the observations, defined as

$$\mathrm{d}_j = \begin{cases} 0 & \text{if } I_j^{\mathrm{o}} - \frac{W_j}{2} \leq I_j^{\mathrm{m}} \leq I_j^{\mathrm{o}} + \frac{W_j}{2} \\ \log_{10}\left(I_j^{\mathrm{m}}\right) - \log_{10}\left(I_j^{\mathrm{o}} - \frac{W_j}{2}\right) & \text{if } I_j^{\mathrm{m}} < I_j^{\mathrm{o}} - \frac{W_j}{2} \\ \log_{10}\left(I_j^{\mathrm{m}}\right) - \log_{10}\left(I_j^{\mathrm{o}} + \frac{W_j}{2}\right) & \text{if } I_j^{\mathrm{m}} > I_j^{\mathrm{o}} + \frac{W_j}{2}, \end{cases} \tag{2.16}$$

where I_j^m is the intensity of the model of line j, I_j^o is the intensity observed of line j and W_j is the uncertainty associated with σ. The distances d_j are squared and summed, effectively calculating the distance in hyperspace between the model and the observation. This results in the total distance

$$\mathrm{d} = \sqrt{\sum_{j=1}^{N} \mathrm{d}_j^2}. \tag{2.17}$$

This equation is a distance equation with unit dex on a logarithmic scale and physically implies that at a dex of 1 at most one observation is underestimated or overestimated by a factor of 10. The best model is the model with the lowest distance. Additionally, results from the model were used as constraints to remove nonphysical models. Models with maximum shock temperatures lower than the temperatures derived from the rotational diagrams were excluded.

Version of June 14, 2024– Created June 14, 2024 - 14:55

Chapter 3

Results

The analysis aimed to find the intensities of the molecular hydrogen emission lines in the JWST MIRI-MRS range and to create rotational diagrams. A full report of the integrated fluxes of all lines is in Appendix B, which are a factor of the solid angle away from the intensities. The calculated intensities and rotational diagrams were used for comparison with the results of the shock model simulation by K23.

3.1 Integrated intensity maps

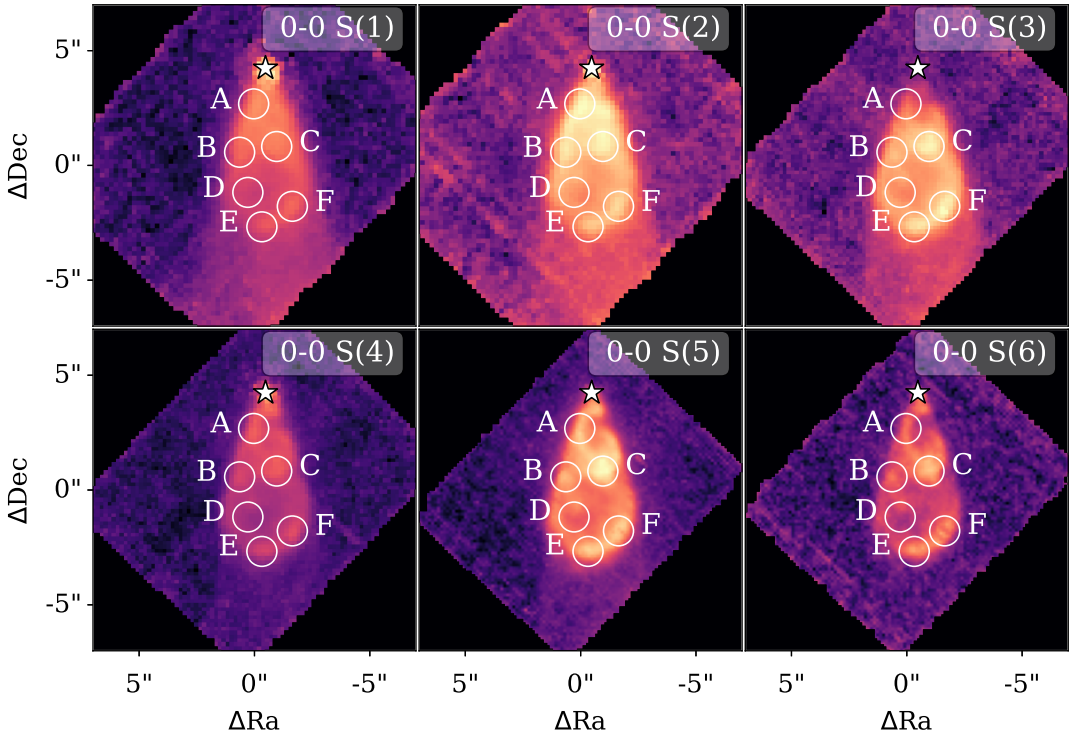

Figure 3.1: *The integrated intensity map for every observed H_2 transition in the outflow. The figures are shown in log-scale. The white circles are the apertures A-F used for spectral analysis. The star is the location of the protostar, based on the location of the highest continuum emission.*

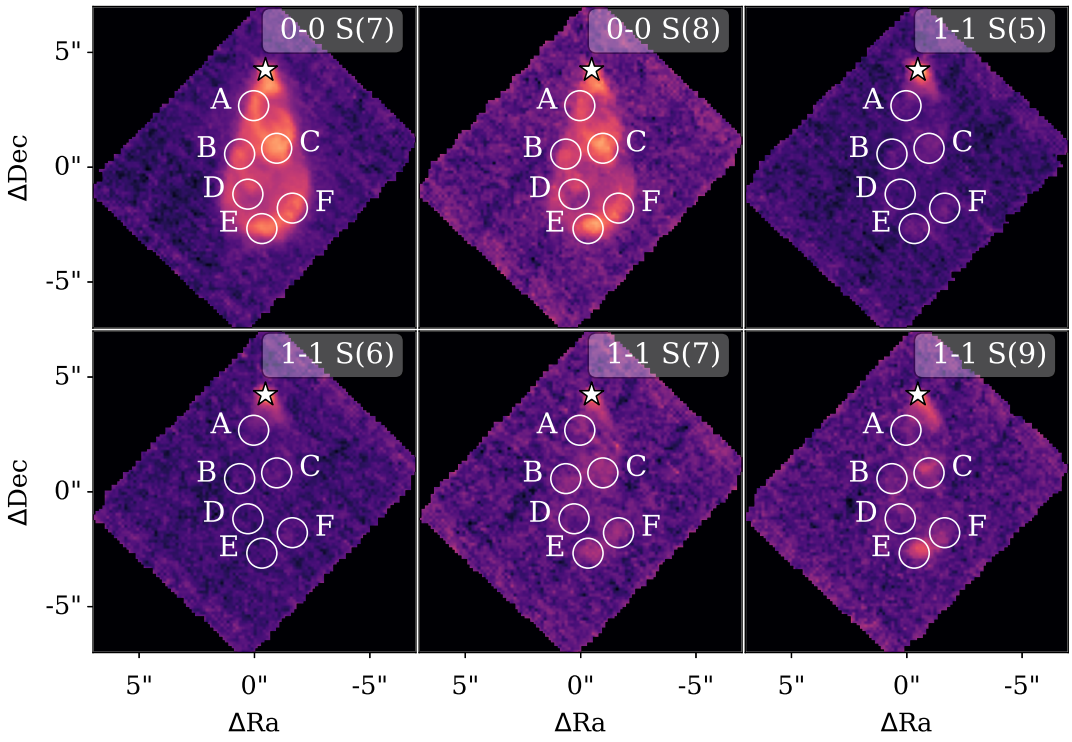

Figure 3.1: *Continued.*

Figure 3.1 shows the integrated intensity maps for all observed H_2 transitions in the outflow. In the 0-0 S(3), S(5), S(7) and S(8) line, a two bow-shaped structures are visible. One bow-shaped region goes through apertures B and C, and a second bow-shaped region can be seen through E and F. The bow shapes are at the locations with the most [Ni II] emission (see Methods 2.2.1), which traces the collimated jet within the outflow. This points to shocks predominantly driven by the jet. These bow shocks are also the areas where the 1-1 lines show the most emission, though they are still very faint. Only 1-1 S(7) and 1-1 S(9) show significant visible emission. In the 0-0 S(1), S(2), S(3), and S(5) a continuation of the outflow is visible, beyond the outer bow shock in this observation. Aperture D is in an area with less emission, which is inconsistent with the [Ni II] tracing the jet.

3.2 Rotational diagrams and fit results

Figure 3.2 shows the rotational diagrams for every aperture. The extinction uncorrected and extinction corrected data are plotted, and the fit is shown as a line through the data points. The uncertainty on the extinction correction is not included in the fit, as it is not an independent uncertainty of each data point but affects all data points simultaneously. However, to indicate the size of the extinction correction, they are plotted as error bars on the intensities. The two temperature components are shown as linear lines using fit parameters from Equation 2.13. This fit was performed for A_K, $A_K + \sigma_{A_K}$ and $A_K - \sigma_{A_K}$, to indicate how large the uncertainty on the column density is due to the extinction uncertainty. Table 3.1 summarises all resulting column densities and temperatures. The column density of the hot component is generally $\sim$ 10% of the column density of the cold component for these outflow positions. The extinction

Version of June 14, 2024– Created June 14, 2024 - 14:55

correction A_K decreases with the distance to the protostellar system, indicating that the envelope gets less dense when moving away from the protostellar system. This is expected considering the envelope density decreases with the distance to the source [58]. The uncertainty of the extinction is biggest in the apertures drawn on the jet (A, C and E). The column densities also decrease with distance, which is expected for the same reason as the decrease in A_K. The temperatures of the warm components vary little, except for aperture A, which is $\sim$ 200K colder. The temperatures of the hot components display significant variations, but all temperatures, warm and hot, fall within the uncertainty of each other.

Table 3.1: *Column densities and temperatures of the six apertures, calculated by fitting equation 2.12 to the rotational diagram. The fit was done for A_K, $A_K + \sigma_{A_K}$ and $A_K - \sigma_{A_K}$.*

Aperture	$N_{warm}(\mathrm{cm}^{-2})$	$T_{warm}(\mathrm{K})$	$N_{hot}(\mathrm{cm}^{-2})$	$T_{hot}(\mathrm{K})$	A_K
			Extinction correction A_K		
A	$4.5 \pm 2.2(+21)$	771 ± 127	$1.4 \pm 1.3(+20)$	2238 ± 398	10.25 ± 1.87
B	$2.4 \pm 0.7(+20)$	938 ± 96	$5.5 \pm 4.5(+18)$	2941 ± 571	4.98 ± 0.23
C	$2.6 \pm 0.6(+20)$	1029 ± 111	$1.4 \pm 1.0(+19)$	2645 ± 417	4.54 ± 1.14
D	$5.9 \pm 1.4(+19)$	979 ± 94	$1.7 \pm 1.3(+18)$	2833 ± 482	3.05 ± 0.23
E	$5.5 \pm 1.2(+19)$	1081 ± 115	$3.4 \pm 2.4(+18)$	2985 ± 498	2.73 ± 0.58
F	$5.8 \pm 0.8(+19)$	1004 ± 79	$3.3 \pm 1.3(+18)$	2649 ± 265	2.22 ± 0.31
			Extinction correction $A_K + \sigma_{A_K}$		
A	$1.2 \pm 0.6(+22)$	767 ± 132	$2.9 \pm 3.0(+20)$	2287 ± 468	10.25 ± 1.87
B	$2.7 \pm 0.7(+20)$	937 ± 96	$6.0 \pm 5.0(+18)$	2955 ± 587	4.98 ± 0.23
C	$4.7 \pm 1.2(+20)$	1026 ± 117	$2.1 \pm 1.8(+19)$	2726 ± 508	4.54 ± 1.14
D	$6.6 \pm 1.5(+19)$	977 ± 95	$1.9 \pm 1.4(+18)$	2848 ± 496	3.05 ± 0.23
E	$7.4 \pm 1.7(+19)$	1080 ± 118	$4.1 \pm 3.1(+18)$	3038 ± 551	2.73 ± 0.58
F	$6.8 \pm 1.0(+19)$	1003 ± 81	$3.6 \pm 1.6(+18)$	2668 ± 280	2.22 ± 0.31
			Extinction correction $A_K - \sigma_{A_K}$		
A	$1.7 \pm 0.9(+21)$	770 ± 132	$7.0 \pm 6.0(+19)$	2184 ± 360	10.25 ± 1.87
B	$2.2 \pm 0.6(+20)$	939 ± 95	$5.1 \pm 4.1(+18)$	2926 ± 556	4.98 ± 0.23
C	$1.5 \pm 0.4(+20)$	1026 ± 115	$9.9 \pm 6.9(+18)$	2560 ± 377	4.54 ± 1.14
D	$5.2 \pm 1.2(+19)$	980 ± 94	$1.6 \pm 1.2(+18)$	2818 ± 470	3.05 ± 0.23
E	$4.1 \pm 0.9(+19)$	1081 ± 115	$2.8 \pm 1.9(+18)$	2931 ± 463	2.73 ± 0.58
F	$4.9 \pm 0.7(+19)$	1005 ± 78	$2.9 \pm 1.2(+18)$	2630 ± 255	2.22 ± 0.31

Notes: *The brackets indicate the order of magnitude: $b(a)$ is $b \times 10^a$.*

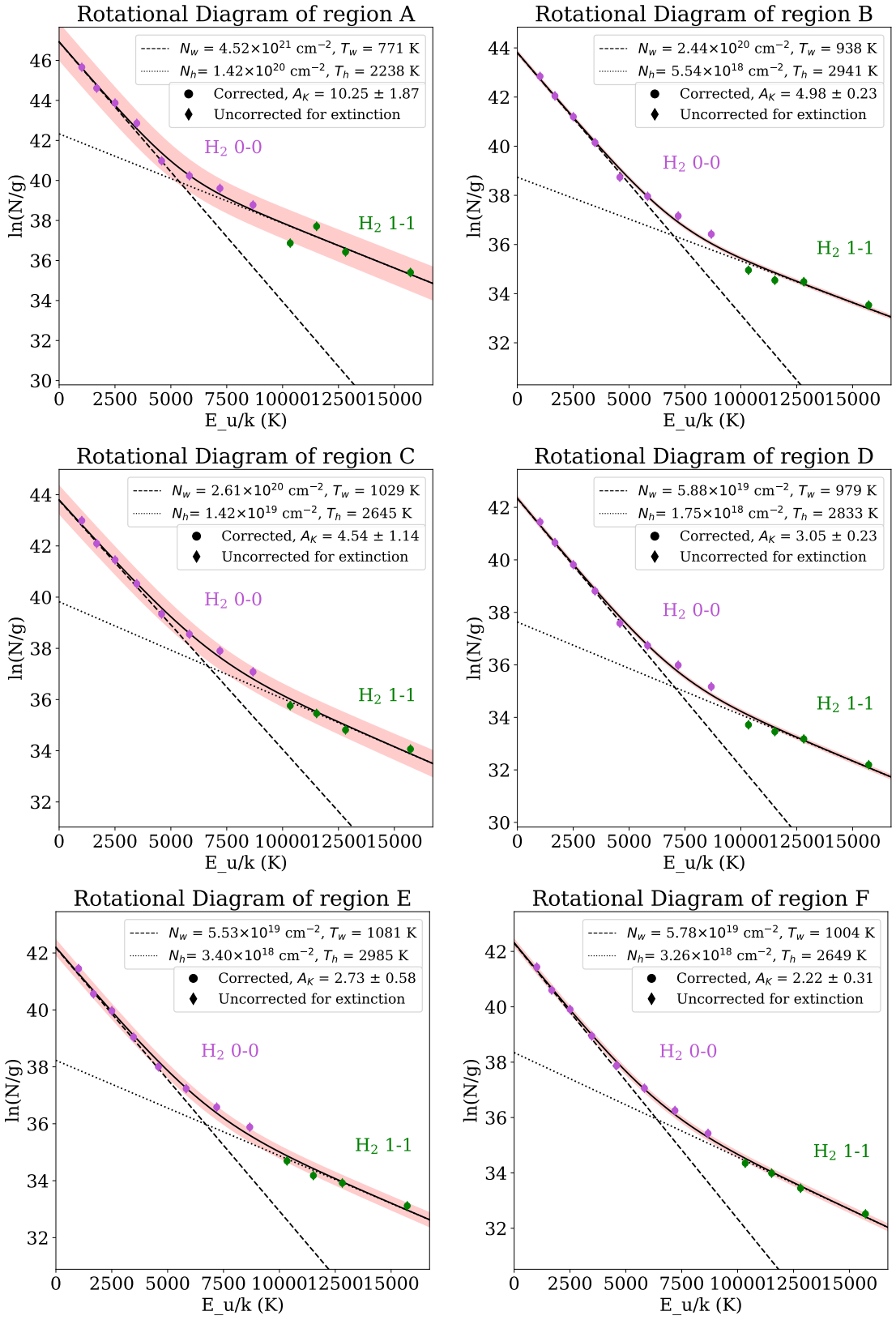

Figure 3.2: *Rotational diagrams of each aperture. Both the uncorrected (diamond markers) and extinction-corrected (dot markers) data points are displayed. The purple markers are the 0-0 transitions, while the green markers are the 1-1 transitions. The solid black line is the best-fit model. The dotted and dashed lines are the hot and warm components, respectively. The red fill shows the uncertainty on the extinction correction. The column densities and the temperature of the fit are shown in the legend and are reported with uncertainty in Table 3.1*

3.3 Comparison to the K23 Model

The minimum distance analysis resulted in 6 best-fit models for each aperture at the calculated extinction. Figure 3.3 shows the observed intensities and the best-fit model intensities are plotted for aperture E, the others are in Appendix D. In Table 3.2 the initial parameters of the models are reported. For each aperture, a best-fit model was found with $d < 1$ dex, i.e. no data point was underestimated or overestimated by a factor larger than 10. Apertures B and C had a best-fit model with an unphysical temperature, i.e. the maximum temperature of the shock $T_{model,max}$ in the model was lower than the temperature of the rotational diagram T_{hot}. In these cases, the next best-fit model was examined, until a model was found with a $T_{model,max} < T_{hot}$. The best-fit models for aperture E and F are, though with different d_{min}, the same except for ζ_{H_2}. Furthermore, the densities decrease, similar to the column densities in the rotational diagrams. On the other hand, the magnetic field scalar b and the shock velocity v_s seem to increase with distance. Note that the magnetic field also scales with the square root of the proton density n_H, so b is not a representative value for the absolute magnetic field strength. The shock velocity is $\geq 50 \text{kms}^{-1}$ for all apertures. This would normally dissociate molecules, but due to the also large magnetic field, the shock may be non-dissociative. A large magnetic field may be consistent with observations by Hull et al.(2020)[59], who find hourglass magnetic field lines characteristic for high magnetic fields, though the magnetic field strength itself has not been measured. This combination of high velocity and high magnetic fields leads to C-type shocks.

However, as there is uncertainty on the extinction correction, we must evaluate the best-fit models within the uncertainties. The extinction uncertainty cannot be used as uncertainty on the intensities, it is not an independent measurement for each data point. Instead, the intensities are extinction corrected for values of A_k between $A_k - \sigma_{A_k} < A_k < A_k + \sigma_{A_k}$. All the unique best-fit models provide restrictions on the initial conditions. The set of restrictions for the initial parameters at each location is shown in Table 3.3. A complete report of all models that fit the data is in Appendix E. Aperture

Table 3.2: *The initial parameters of the models that resulted in the lowest dex for each aperture.*

Aperture	d_{min} (dex)	$n_H^{(a)}$ (cm^{-3})	v_s(kms^{-1}	$b^{(b)}$	$G_0^{(c)}$	$\zeta_{H_2}^{(d)}$	$X(PAH)$	Shock Type
A	0.553	10^8	50.0	3.0	0.1	10^{-17}	10^{-6}	CJ
B$^{(e)}$	0.731	10^4	50.0	3.0	10.0	10^{-15}	10^{-7}	C
C$^{(e)}$	0.475	10^4	60.0	3.0	0.0	10^{-15}	10^{-6}	C
D	0.387	10^3	80.0	10.0	10.0	10^{-15}	10^{-6}	C
E	0.359	10^3	90.0	10.0	10.0	10^{-17}	10^{-6}	C
F	0.238	10^3	90.0	10.0	10.0	10^{-15}	10^{-6}	C

Notes: *$^{(a)}$Proton density $n_H = n(H) + 2n(H_2)$. $^{(b)}$b is a scaling factor for the transverse magnetic field, $B = b \times \sqrt{n_H(cm^{-3})}\mu G$. $^{(c)}G_0$ in units of the field from Mathis et al. 1983. $^{(d)}H_2$ cosmic-ray ionisation rate. $^{(e)}$Although aperture B and C had best-fit models with lower d_{min} than shown here, those models had a lower T_{max} than the measured temperature from the rotational diagrams and were therefore excluded.*

Table 3.3: *Number of models for each parameter and the restrictions that they impose on the physical initial conditions. ζ_{H_2} is not shown, see Discussion 4.4. A dash (-) denotes a range, and a slash (/) denotes alternatives.*

Aperture	# models	$n_H^{(a)}\mathrm{cm}^{-3}$	$v_s(\mathrm{kms}^{-1})$	b$^{(b)}$	G0$^{(c)}$	$X(PAH)$	Shock type
A	19	$10^7 - 10^8$	$50 - 90$	3-10	-	-	CJ
B	3	$10^4/10^7$	50-60	3	10/1000	$10^{-7}/10^{-6}$	C
C	8	$10^4 - 10^5$	$30 - 90$	3-10	0-100	-	C
D	3	10^3	60/80	3-10	10	$10^{-7}/10^{-6}$	C
E	4	$10^3 - 10^4$	$40 - 90$	3-10	10-100	$10^{-7}/10^{-6}$	C
F	2	10^3	90	10	10	10^{-6}	C

Notes: *$^{(a)}$Proton density $n_H = n(H) + 2n(H_2)$. $^{(b)}$b is a scaling factor for the transverse magnetic field, $B = b \times \sqrt{n_H(cm^{-3})}\mu G$. $^{(c)}G_0$ in units of the field from Mathis et al. 1983. $^{(d)}H_2$ cosmic-ray ionisation rate.*

A accepts the most models, as is expected since it has the largest uncertainty on the extinction. Still, the density is well constrained, as is the transverse magnetic field. This trend continues for the other apertures, which also show good constraints for the external UV radiation. Velocities are less constrained, though the models exclude low-velocity shocks (< 50 km s^{-1}), except one model with $v_s = 30\mathrm{kms}^{-1}$. All models for each aperture point to the C-type shock, except for aperture A, which points to a CJ-type shock, due to high-velocity and high-density shocks.

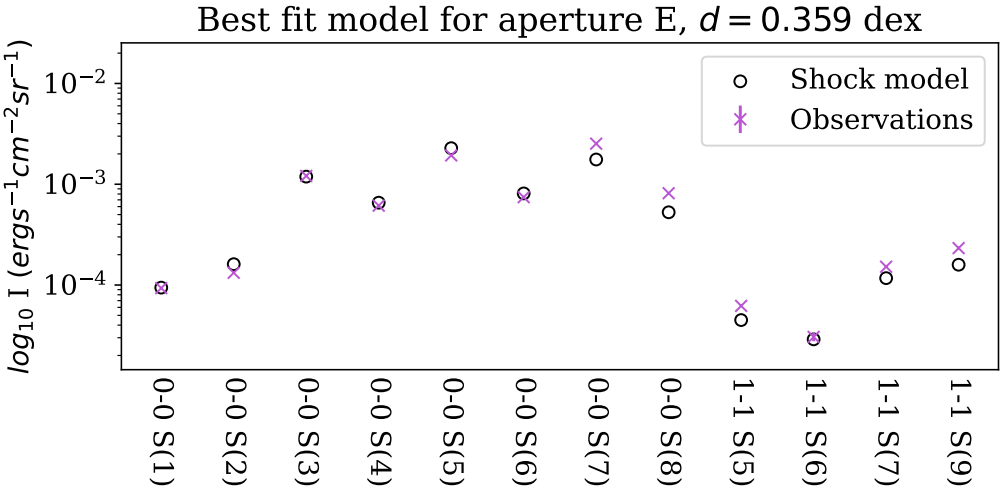

Figure 3.3: *Example of a best-fit model using the minimum distance defined in Section 2.3. The minimum distance is 0.359 dex. The intensities are plotted on a logarithmic axis, and the best-fit model is shown as open black circles. The uncertainty on the intensity is very small, which is amplified by the log scale and the fact that the intensities are corrected for extinction. The x-axis shows the transitions associated with the intensities.*

Version of June 14, 2024– Created June 14, 2024 - 14:55

3.4 Results summary

To visualise the results for the different apertures, Figure 3.4 shows the grey-scale integrated intensity map for the 0-0 S(5) transition with a coloured overlay of the apertures. The colours correspond to the value of the presented quantity from the best-fit models. This way, the trends are visible for the different outflow positions. The temperatures decrease slightly with the distance to the protostellar system, except for the hot component of aperture B, which is high with respect to its neighbours. The total column densities from the rotational diagrams do visibly decrease with distance, as do the densities from the best-fit shock model. The trends are similar. The shock velocity and the transverse magnetic field strength both increase for the best-fit models, however, they are not well constrained following from the models accepted within the extinction correction uncertainty.

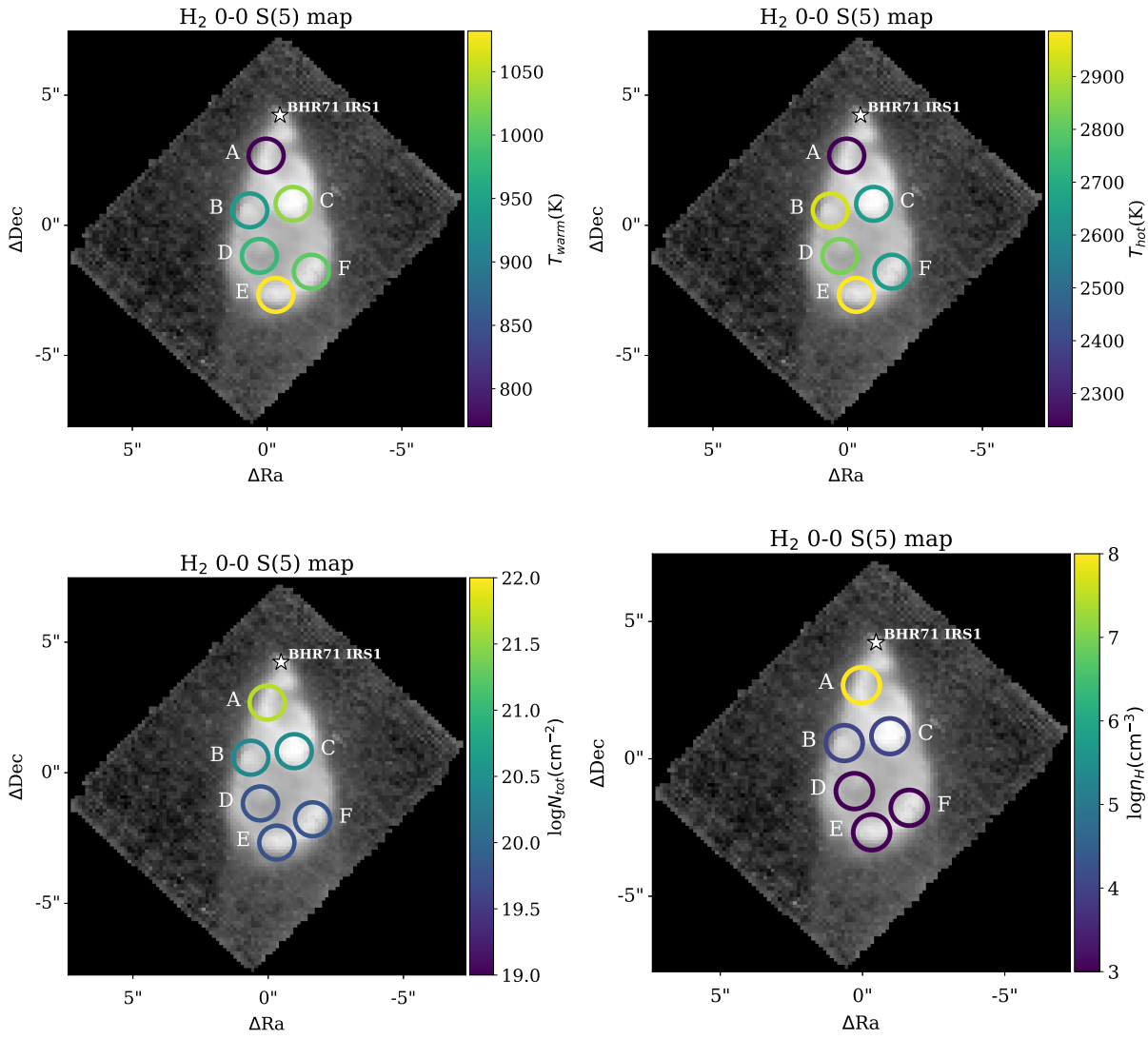

Figure 3.4: *Grey-scale integrated intensity map for the 0-0 S(5) transition with a coloured overlay of the apertures. The colours correspond to the value of the presented quantity from the best-fit models. Exact values are reported in Tables 3.1 and Table 3.2 of the Results section.*

Version of June 14, 2024– Created June 14, 2024 - 14:55

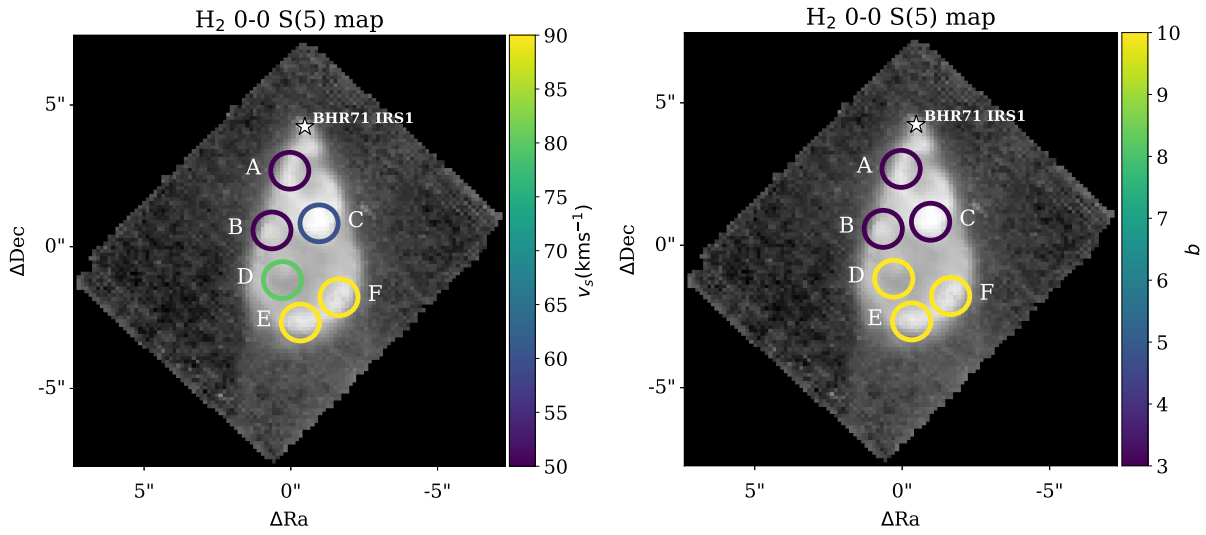

Figure 3.4: *continued*

Chapter 4

Discussions

4.1 Comparison to previous observations

Before the JWST, valuable information about protostellar outflows was gathered with other space telescopes, such as Spitzer and ISO by e.g. Rosenthal et al.(2000)[60], Giannini et al.(2001)[61] and Neufeld et al.[62–64]. Their spectroscopic abilities revealed hidden processes hidden in the envelopes. The combined effort of the previous and current generation of telescopes set the stage for the JWST to explore the outflows in exceptional detail. JWST has the power to spatially resolve previously unresolved emissions with Spitzer, allowing for an unprecedented detailed analysis of the outflow in closer proximity to the protostar. We compare the results from this thesis with observations from the previous generation telescopes, in order to put them into context and find the differences between new and old observations.

Neufeld et al. (2006)[62] analysed the Spitzer observations of 2 Herbig-Haro (HH) objects, clouds of hot gas outside the envelope from protostellar systems. These clouds are shocked by the protostellar jets and radiate the energy away, similar to the molecular hydrogen close to the protostar. The objects observed with Spitzer were HH7 and HH54, shocked by the very early Class I protostar SVS13 [65]. The HH objects are powered by the molecular bullets from the protostar. Spectra were obtained by creating apertures with a radius of 15″ and their rotational diagrams were fitted with a two-component fit. Three apertures were drawn for HH54. The results were temperatures of 382K$<$ T_{warm} $<$ 558K and 1025K$<$ T_{hot} $<$ 1150K. They found column densities of the order 10^{20} cm^{-2} for the warm component and 10^{19}cm^{-2} for the hot component. The column densities are comparable to those found for the outer locations in the BHR71 outflow. In addition, they find densities of H_2 of $10^4 - 10^5$cm^{-3}. This is consistent with aperture B and C, and higher than D, E and F, but for the latter three, we also find lower column densities. This combination of matching H_2 density and column density points to a similar source for the emission, which is the protostellar jet for the HH objects. Furthermore, the matching density points to the fact that the outflow cavity away from the protostellar system has hydrogen densities comparable to the entire molecular cloud. The temperatures for their hot components are comparable to our cold components. They only used the 0-0 rotational transitions, whereas we have access to 1-1 transitions, the latter of which dominate the hotter component. In addition, they had access to the 0-0 S(0) line, the lowest E_u line of H_2 which is most

Table 4.1: *Physical conditions obtained from the best-fit models to the observations. Δz is the shock width.*

Aperture	$N(H_2)$ (cm^{-2})	T_{max} (K)	o/p_{ini}	N_o/N_p	Δz(AU)
A	$1.37 \cdot 10^{22}$	59340.0	0.04	2.02	38
B	$1.69 \cdot 10^{20}$	4776.0	0.1	2.75	724
C	$4.60 \cdot 10^{20}$	8159.0	0.15	2.01	1700
D	$9.22 \cdot 10^{19}$	5947.0	0.51	2.26	6200
E	$8.21 \cdot 10^{19}$	8727.0	2.11	2.88	5170
F	$8.04 \cdot 10^{19}$	8647.0	0.51	2.29	5110

sensitive to colder material. Taking that into account, their hot and our warm components use almost the same transitions, which might explain the similarity in those temperatures.

Neufeld et al. (2009)[63] investigated 5 protostellar systems, one of which was BHR71 IRS1. They stitched together 4 $\sim 1' \times 1'$ regions arranged along the outflow around IRS1 and IRS2, which they extracted and summed to obtain one spectrum, compared to our aperture radius of 0.65″. Their best-fit model resulted in $\log_{10}(n_H) = 3.8 \pm 0.4$ and an initial H_2 OPR of ≤ 2.4 with a confidence of 95%. Both the jet and the wider outflow contribute to this density calculation. The hydrogen density is in agreement with our outer location apertures' densities. Apertures A and B show a higher density, but this is at a resolution Spitzer cannot resolve. The initial OPR was reported to be ≤ 2.4, and we find similar results. Table 4.1 shows that the initial o/p_{ini} is below 2.4 for every aperture. In an additional paper (Giannini et al. (2011)[66]) they find an average column density of 10^{20} for the BHR71 IRS1 outflow, with a variation of $3 \cdot 10^{19} - 2 \cdot 10^{20}$. They also find temperatures for the warm component and for the hot component of 310K and 1500K respectively. This is significantly lower than reported in this thesis, pointing to more energetic shocks closer to the protostar. However, they find a higher density of H_2, $\sim 10^6 cm^{-3}$, which may explain the similarity in column density.

Lastly, Neufeld et al. (2019)[64] observed HH7, but with the Stratospheric Observatory for Infrared Astronomy (SOFIA) instrument Echelon-Cross-Echelle Spectrograph (EXES). They compared the intensities of the 0-0 S(4), S(5), S(6) and S(7) line with the Paris-Durham shock model (the same model that was used by K23) to find a C-type shock with $n_H = 10^4 cm^{-2}$, $v_s = 25 km\ s^{-1}$ and b = 1.3. Their best-fit shock velocity and transverse magnetic field are slightly lower, which could be attributed to the fact that the HH object is farther away from the protostellar system and to the fact that SVS13 is a Class I protostar with a less powerful jet. Generally, the new observations agreed well with older, less precise observations from Spitzer and SOFIA.

4.2 Comparison with other JWST observations

BHR71 is not the only object observed within the JOYS program, other objects have also been observed with both MIRI MRS and NIRSpec. An example is the Class I binary system TMC1, which consists of two young stellar objects TMC1-W and TMC1-E analysed by Tychoniec et al.(2024)[46]. TMC1-W launches a collimated jet, while TMC1-E has a disk wind outflow. The wind spectrum has been analysed and was found to excite H_2 to temperatures $T_{warm} = 661$K and $T_{hot} = 1849$K with column densities of $N_{warm} = 10^{19}\text{cm}^{-2}$ and $N_{hot} = 10^{18}\text{cm}^{-2}$. The jet from TMC1-E has negligible influence on the H_2 intensities. This lower temperature and column density close to the protostellar system can be attributed to the less powerful Class I jets and Class I wind outflow, marking a later stage in the star formation process. This difference between the outflows from Class 0 and Class I protostars can be studied further in the future by comparing a larger sample of targets at different evolutionary stages.

More H2 observations with JWST MIRI within the JOYS program were analysed by Gieser et al. (2023, corrected 2024)[67]. They studied the high-mass IRAS23385+6053 cluster, which consists of four continuum sources and three bipolar outflows. Although the sources are unknown, they find both C-type and J-type shocks for the outflows. There are no clear differences in their rotational diagram between regions excited by either shock. They have calculated column densities and temperatures using rotational diagrams for $A_K = 3, 5, 7$, as they cannot calculate the best-fit value for A_K using completely resolved MIRI lines. The temperatures are generally lower for all extinctions than reported in this thesis, while the column densities are higher. This may be attributed to the higher densities in that cloud ($\sim 10^7\text{cm}^{-3}$[68]) or a larger outflow, considering the high-mass objects.

The Investigating Protostellar Accretion (IPA) is another program from the JWST Cycle 1. Within this program, Narang et al.(2024)[69] analysed observations of the low-luminosity Class 0 protostar IRAS16253-2429. It has a bolometric luminosity of $L_{bol} = 0.2L_\odot$ and a relatively low mass-loss and mass accretion rate. The bolometric temperatures of BHR71 IRS1 and IRAS16253-2429 are roughly the same, so assuming that bolometric luminosity quantifies heating that is provided by the protostellar accretion to the system, we find that BHR71 IRS1 heats its environment much more. This is reflected in the rotational diagram results from the IRAS16253-2429 jet. The warm temperatures and hot temperatures reported are $\sim 500 - 700$K and $\sim 700 - 800$K respectively. The hot component is ~ 3 times lower than reported for BHR71 IRS1. This may be attributed to the lower luminosity and low mass loss, but this can be confirmed by comparing the temperatures to other Class 0 protostars in future research.

The Project-J program shows promising results for the observation of HH46 IRS by Nisini et al.(2024) [70]. HH46 IRS is a Class I binary protostellar system. Papers are in the work for the complete analysis of H_2 detected with MIRI in this source, which might provide additional insights into shocked molecular hydrogen around protostars.

In order to make these comparisons work it is important to note that the JOYS papers also made use of the McClure (2009)[44] extinction law, while Narang et al.(2024)

used the KP5 extinction law. KP5 is a widely used extinction law, which has been in use since 2009 but has recently been documented [71]. According to this paper, KP5 is the best available extinction correction curve. Comparisons to the other papers made the use of McClure as the preferred extinction law, but for future work, the KP5 extinction curve can be incorporated into the analysis.

4.3 Comparison of $N(H_2)$ from the shock model and the rotational diagram

The upper panel of Figure 4.1 shows the total column density from the rotational diagram and the column density calculated in the simulation for the best-fit models. For every aperture, the column density from the rotational diagram is smaller than the column density from the model. One explanation is the absence of the lowest excitation H_2 transition 0-0 S(0), which would have added a cold component and could close the gap. Another possibility is that the assumption of LTE is not valid. Rotational diagrams assume local LTE, which might affect the correctness of the rotational diagram. The OPR is one characteristic of the conditions that can be examined for LTE. If the medium is in LTE and $T > 200$K, the OPR of molecular hydrogen is 3[72]. The lower panel of Figure 4.1 shows the OPR for the sources and Table 4.1 reports the exact values. There is no big deviation from this value in the apertures, except aperture A. This aperture is closest to the protostar, which might affect the OPR due to the feedback mechanisms. Overall, we cannot distinguish between LTE and non-LTE based on the OPR values.

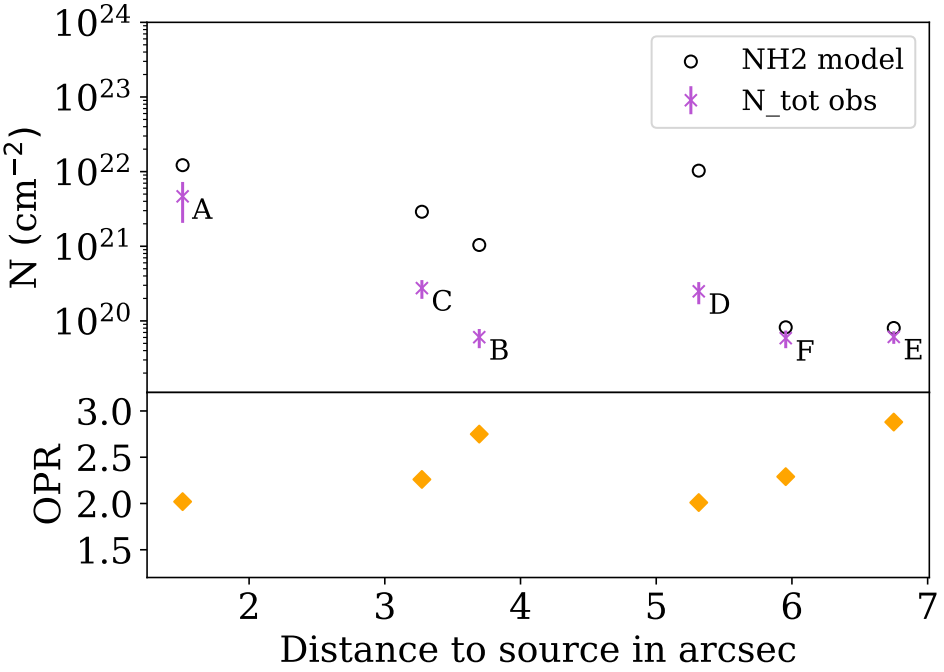

Figure 4.1: *The rotational diagram column density compared to the calculated column density from the best-fit model. The upper panel shows the logarithmic values of the observation and the model, while the lower panel shows the mean OPR of all best-fit models of that aperture. The x-axis shows the absolute distance to the source in arcseconds.*

4.4 The impact of ζ_{H_2}, $X(PAH)$ and G_0

K23 uses 6 initial parameters for the medium to simulate the shocks, namely n_H, v_s, b, G_0, ζ_{H_2} and $X(PAH)$. The first four significantly change the resulting H_2 line intensities, but ζ_{H_2} and $X(PAH)$ barely impact the predicted line intensities of the model. Figure 4.2 shows the minimum distance in dex for models around the best-fit model. One initial condition was varied, while all others were kept constant, and the minimum distance was calculated. Although $X(PAH)$ has a slight preference for one model, ζ_{H_2} has a near-constant minimum distance. The variance in ζ_{H_2} is $< 3 \cdot 10^{-3}$ dex^2, with a minimum as low as $8 \cdot 10^{-9}$ dex^2 for aperture C. For comparison, the variance for n_H is > 4 dex^2 with a peak at 37.5 dex^2 for aperture C. $X(PAH)$ shows a slight preference for one model or a slight disfavour for one model, which is significant enough to be taken into account. All best-fit models prefer a $X(PAH)$ of 10^{-6}, except for the model fitted to aperture B. For aperture A, most likely a high-density CJ shock, G_0 is of relative unimportance, but for the other apertures G_0 does impact the minimum distance.

4.5 Grid of 4D parameter space

In K23, they provide a grid in the 4D parameter space, where they keep ζ_{H_2} and X(PAH) fixed to show the resulting shock types for certain initial conditions. We recreated this grid to show in which regions of 4D space the minima in the distance between the model and the observations are. This was done only for intensities corrected using the derived A_K, not for all A_K within the uncertainty. The colour in the grid is based on the value in the grid, which is the distance in units of (dex) given by equation 2.16. Higher distances are purple while lower distances (better models) are yellow, with green as a transition colour. The colours are capped at the median distance, to visualise where the better models are. The grid can be used to reduce the parameter space in order to simulate shock models using finer initial conditions. Figure 4.3 shows this grid for aperture A. Low-velocity shocks can immediately be excluded from further analysis. The grid points to a high-density, high-velocity shock with a preference for a G_0 of 0.1-10 (units as before). The grids for the other models are in Appendix F. The grids are mostly consistent with the ranges of values found for the initial conditions within the extinction uncertainty. Important to note is that the grid does not distinguish between physical and unphysical models at this point. Low minimum distance models may have $T_{max} < T_{hot}$.

4.6 Resolving shocks

With the JWST, the spatial resolution has improved greatly. Assuming a distance of 150 parsecs[31, 32], the projected diameter of an aperture is $\sim$ 195AU. Physical lengths of shocks can vary between several tens of AU to several hundreds of AU [73]. In addition, shocks can display bullet-like behaviour, which could lead to multiple shocks in one aperture. Table 4.1 reports the width of the shock in AU simulated by the shock model, defined as the extent of the region where 80 % of the emission is radiated away. These values, except for aperture A, are not physical for this outflow. This may follow from an assumption in the shock code or because the apertures cover both the jet and the cavity outflow, resulting in higher radiation. Still, the models predict large shock widths, pointing to the fact that we may only see at most one shock per aperture.

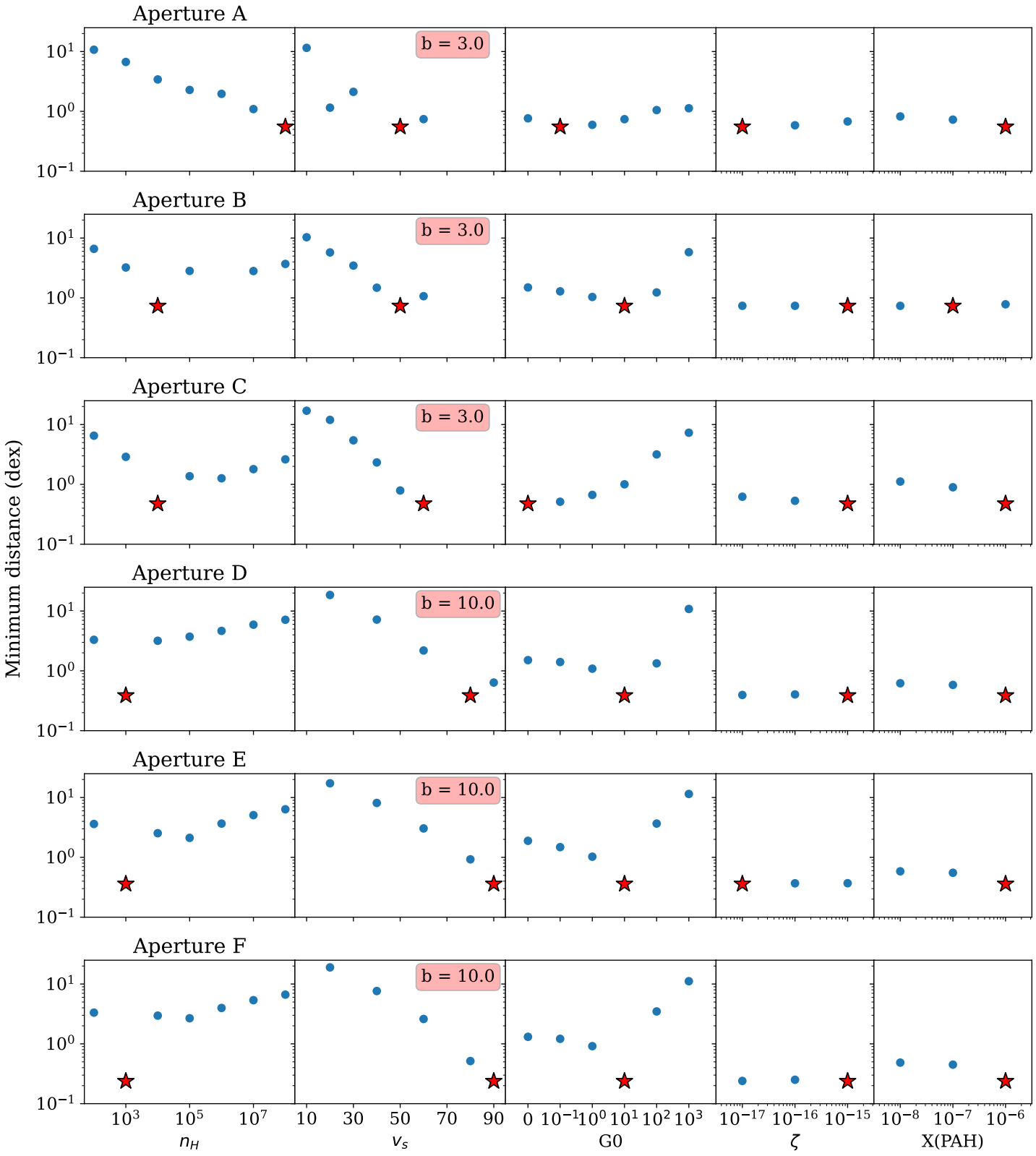

Figure 4.2: *The minimum distance around the best-fit model. While each initial parameter was varied, the others were kept constant at their best-fit value. Missing points are caused either because the grid is limited or because the shock model returned 0 for all intensities. The red star indicates the best-fit model value. As the magnetic field and shock velocity are coupled in the initial grid, the magnetic field was kept constant and only the shock velocity was varied.*

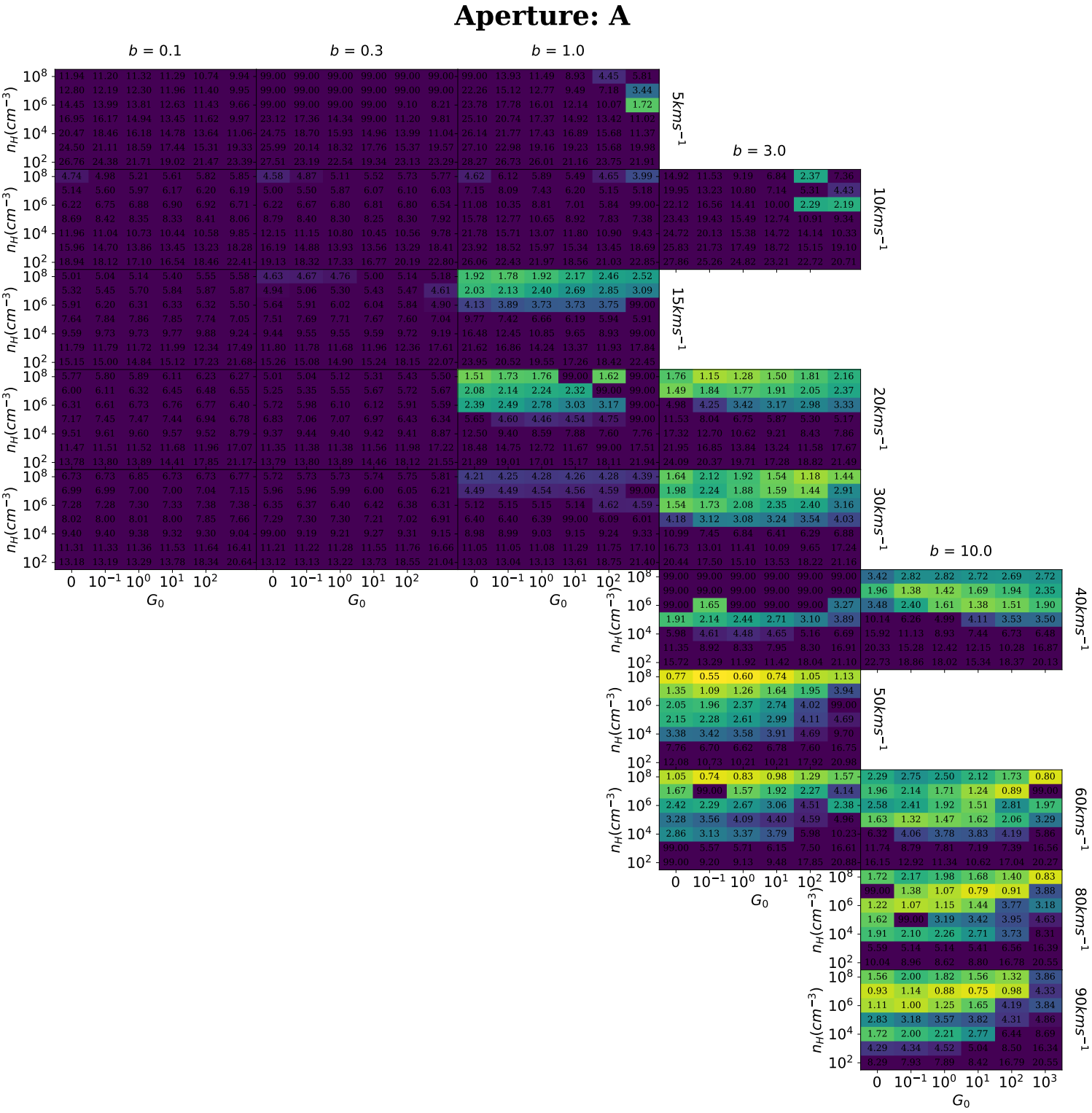

Figure 4.3: *4D grid of Aperture A with distances between models and the observation. ζ_{H_2} and $X(PAH)$ are set to their best-fit model values, which for Aperture A are $\zeta_{H_2} = 10^{-17}$ and $X(PAH) = 10^{-6}$. The colour is based on the value in the grid, which is the distance in units of (dex) given by equation 2.16. Higher distances are purple while lower distances (better models) are yellow, with green as a transition colour. The colours are capped at the median distance, to visualise where the better models are.*

Version of June 14, 2024– Created June 14, 2024 - 14:55

4.7 Future work

The results obtained for this thesis can be used to do a more in-depth search with the shock model. The grids can be used as pointers for initial parameter ranges and may be recreated for other outflow positions or objects, as it is computationally inexpensive. Another way of increasing the certainty about molecular outflows is observations using the NIRSpec instrument, which provides access to the rovibrational transitions of H_2 compared to only the rotational lines. Results can be used to compare outflows from Class 0 protostars to Class I protostars, which are also currently being observed with the JWST. This may provide more information on the formation and feedback mechanics behind protostellar systems.

Version of June 14, 2024– Created June 14, 2024 - 14:55

Chapter 5

Conclusions

In this thesis, we looked toward the protostellar system BHR71 IRS1 and analysed the outflow, which was observed in unprecedented detail using the JWST/MIRI MRS instrument. We see 12 rotational transitions of H_2 at different locations in the outflow, which trace shocks from the jet and cavity walls. Our key findings are summarised as follows:

1. The H_2 intensities observed at different locations in the protostellar outflow all point to C-type shocks, though with varying pre-shock densities and shock velocities. This is in agreement with a previous study of a jet-shocked Herbig-Haro object. Only aperture A, which is the closest to the protostar, finds a CJ-type shock, likely due to the higher density. Pre-shock densities are well constrained and tend to increase toward the protostar, while best-fit shock velocities tend to increase away from the protostar. However, shock velocities are not well constrained due to the uncertainty on the extinction, resulting in $v_s \geq 50\text{kms}^{-1}$, except one model that finds $v_s = 30\text{kms}^{-1}$. The magnetic field strength is consistently high with values of b = 3 and b = 10, where b is a scaling factor for $B = b \times \sqrt{n_H(cm^{-3})}\mu G$, in agreement with previous observations. The best-fit models indicate that the scalar increases away from the protostar, but this is not well constrained.

2. We find relatively high temperatures of $T_{warm} \sim 1000\text{K}$ and $T_{hot} \sim 2600\text{K}$ in the outflow close to the protostar compared to previous observations by Spitzer of a $4' \times 1'$ area of the outflow. However, they found a higher average density than we did for distant outflow positions, pointing to a lower density in the cavity close to the protostar. This may explain the similar column densities observed of around $N_{warm} \sim 10^{20}\text{cm}^{-2}$ and $N_{hot} \sim 10^{19}\text{cm}^{-2}$. The high temperatures indicate that the shocks might predominantly be caused by the jet.

3. Compared to a Class I outflow analysed by Tychoniec et al.(2024) we find higher column densities and temperatures close to the protostar, consistent with the paradigm of more energetic outflows in Class 0 protostars.

4. The analysis from this thesis is a good starting point for additional research into the outflows close to the central protostar. MIRI MRS can very well constrain initial conditions for protostellar outflows using the shock model published by Kristensen et al.(2023). The minimum distance grid provides initial conditions

for the simulation of shock codes with a finer grid, and using additional observations from NIRSpec we could constrain the conditions further, using similar analyses as presented here.

Bibliography

[1] A. T. Barnes, S. N. Longmore, C. Battersby, J. Bally, J. M. D. Kruijssen, J. D. Henshaw, and D. L. Walker, *Star formation rates and efficiencies in the Galactic Centre*, **469**, 2263 (2017).

[2] M. R. Krumholz, M. R. Bate, H. G. Arce, J. E. Dale, R. Gutermuth, R. I. Klein, Z. Y. Li, F. Nakamura, and Q. Zhang, *Star Cluster Formation and Feedback*, in *Protostars and Planets VI*, edited by H. Beuther, R. S. Klessen, C. P. Dullemond, and T. Henning, pages 243–266, 2014.

[3] C. D. Matzner, *Protostellar Outflow-driven Turbulence*, The Astrophysical Journal **659**, 1394 (2007).

[4] J. Bally, *Protostellar Outflows*, **54**, 491 (2016).

[5] L. S. Sparke and I. Gallagher, John S., *Galaxies in the Universe: An Introduction*, 2007.

[6] E. Herbst, *Chemistry in the Interstellar Medium*, Annual Review of Physical Chemistry **46**, 27 (1995).

[7] L. E. Kristensen, B. Godard, P. Guillard, A. Gusdorf, and G. Pineau des Forêts, *Shock excitation of H_2 in the James Webb Space Telescope era*, **675**, A86 (2023).

[8] A. G. G. M. Tielens, *The Physics and Chemistry of the Interstellar Medium*, 2010.

[9] R. C. Kennicutt and N. J. Evans, *Star Formation in the Milky Way and Nearby Galaxies*, **50**, 531 (2012).

[10] G. B. Field, D. W. Goldsmith, and H. J. Habing, *Cosmic-Ray Heating of the Interstellar Gas*, **155**, L149 (1969).

[11] Y. Fukui and A. Kawamura, *Molecular Clouds in Nearby Galaxies*, **48**, 547 (2010).

[12] M. Barsony, S. J. Kenyon, E. A. Lada, and P. J. Teuben, *A Near-Infrared Imaging Survey of the ρ Ophiuchi Cloud Core*, **112**, 109 (1997).

[13] B. A. Wilking and C. J. Lada, *The discovery of new embedded sources in the centrally condensed coreof the rho Ophiuchi dark cloud : the formation of a bound cluster ?*, **274**, 698 (1983).

[14] J. H. Jeans and G. H. Darwin, *I. The stability of a spherical nebula*, Philosophical Transactions of the Royal Society of London. Series A, Containing Papers of a Mathematical or Physical Character **199**, 1 (1902).

[15] Ł. Tychoniec, *Protostellar jets and planet-forming disks: witnessing the formation of Solar System analogues with interferometry*, PhD thesis, University of Leiden, Netherlands, 2021.

[16] M. V. Persson, *Observations of warm water in young solar-system analogs: Origin, abundances and deuterium fractionation*, PhD thesis, University of Copenhagen, Denmark, 2013.

[17] A. Verliat, P. Hennebelle, A. J. Maury, and M. Gaudel, *Formation of protoplanetary disk by gravitational collapse of a non-rotating*, in *SF2A-2019: Proceedings of the Annual meeting of the French Society of Astronomy and Astrophysics*, edited by P. Di Matteo, O. Creevey, A. Crida, G. Kordopatis, J. Malzac, J. B. Marquette, M. N'Diaye, and O. Venot, page Di, 2019.

[18] S. Bontemps, P. Andre, S. Terebey, and S. Cabrit, *Evolution of outflow activity around low-mass embedded young stellar objects*, **311**, 858 (1996).

[19] M. Narang et al., *Discovery of a Collimated Jet from the Low-luminosity Protostar IRAS 16253â2429 in a Quiescent Accretion Phase with the JWST*, **962**, L16 (2024).

[20] R. Alexander, I. Pascucci, S. Andrews, P. Armitage, and L. Cieza, *The Dispersal of Protoplanetary Disks*, in *Protostars and Planets VI*, edited by H. Beuther, R. S. Klessen, C. P. Dullemond, and T. Henning, pages 475–496, 2014.

[21] A. Karska, *Feedback from deeply embedded low- and high-mass protostars. Surveying hot molecular gas with Herschel.*, PhD thesis, Leiden Observatory, 2014.

[22] C. J. Lada and B. A. Wilking, *The nature of the embedded population in the rho Ophiuchi dark cloud : mid-infrared observations.*, **287**, 610 (1984).

[23] A. C. Raga, J. Canto, L. Binette, and N. Calvet, *Stellar Jets with Intrinsically Variable Sources*, **364**, 601 (1990).

[24] Y. Hu, S. Xu, J. M. Stone, and A. Lazarian, *Turbulent Magnetic Field Amplification by the Interaction of a Shock Wave and Inhomogeneous Medium*, **941**, 133 (2022).

[25] D. R. Flower and G. Pineau Des Forêts, *Excitation and emission of H2, CO and H2O molecules in interstellar shock waves*, **406**, 1745 (2010).

[26] B. T. Draine, *Interstellar shock waves with magnetic precursors*, **241**, 1021 (1980).

[27] W. G. Roberge and B. T. Draine, *A New Class of Solutions for Interstellar Magnetohydrodynamic Shock Waves*, **350**, 700 (1990).

[28] D. F. Chernoff, D. J. Hollenbach, and C. F. McKee, *Magnetohydrodynamic Shocks in the Interstellar Medium*, in *NASA Conference Publication*, edited by D. J. Hollenbach and J. Thronson, Harley A., volume 3084 of *NASA Conference Publication*, page 235, 1990.

[29] J. H. Black and E. F. van Dishoeck, *Fluorescent Excitation of Interstellar H 2*, **322**, 412 (1987).

[30] K. J. Seidensticker and T. Schmidt-Kaler, *The distance and structure of the Coalsack. II. Analysis.*, **225**, 192 (1989).

[31] W. J. B. Corradi, G. A. P. Franco, and J. Knude, *Physical association between the Southern Coalsack and the Chamaeleon-Musca dark clouds.*, **326**, 1215 (1997).

[32] L. Å. Nyman, *The Southern Coalsack*, in *Handbook of Star Forming Regions, Volume II*, edited by B. Reipurth, volume 5, page 222, 2008.

[33] Y.-L. Yang, J. D. Green, N. J. E. II, J.-E. Lee, J. K. Jørgensen, L. E. Kristensen, J. C. Mottram, G. Herczeg, A. Karska, O. Dionatos, E. A. Bergin, J. Bouwman, E. F. van Dishoeck, T. A. van Kempen, R. L. Larson, and U. A. Yildiz, *CO in Protostars (COPS): Herschel-SPIRE Spectroscopy of Embedded Protostars*, The Astrophysical Journal **860**, 174 (2018).

[34] J. J. Tobin, T. L. Bourke, S. Mader, L. Kristensen, H. Arce, F. Gueth, A. Gusdorf, C. Codella, S. Leurini, and X. Chen, *The Formation Conditions of the Wide Binary Class 0 Protostars within BHR 71*, The Astrophysical Journal **870**, 81 (2019).

[35] J. D. Green et al., *Embedded protostars in the dust, ice, and gas in time (digit) Herschel key program: continuum seds, and an inventory of characteristic far-infrared lines from pacs spectroscopy*, The Astrophysical Journal **770**, 123 (2013).

[36] L. E. Kristensen et al., *Water in star-forming regions with Herschel (WISH). II. Evolution of 557 GHz 1_{10}-1_{01} emission in low-mass protostars*, **542**, A8 (2012).

[37] T. L. Bourke, G. Garay, K. K. Lehtinen, I. Köhnenkamp, R. Launhardt, L.-Å. Nyman, J. May, G. Robinson, and A. R. Hyland, *Discovery of a Highly Collimated Molecular Outflow in the Southern Bok Globule BHR 71*, **476**, 781 (1997).

[38] T. Kushwahaa, M. N. Drozdovskaya, L. Tychoniec, and B. Tabone, *ALMA ACA study of the H2S/OCS ratio in low-mass protostars*, Astronomy amp; Astrophysics **672**, A122 (2023).

[39] L. A. Zapata, M. Fernández-López, L. F. Rodríguez, G. Garay, S. Takahashi, C.-F. Lee, and A. Hernández-Gómez, *ALMA Reveals a Collision between Protostellar Outflows in BHR 71*, **156**, 239 (2018).

[40] I. Argyriou et al., *JWST MIRI flight performance: The Medium-Resolution Spectrometer*, **675**, A111 (2023).

[41] I. Argyriou, *Calibration of the MIRI instrument on board the James Webb Space Telescope*, Phd thesis, KU Leuven, 2021, Available at `https://fys.kuleuven.be/ster/pub/phd-thesis-yannis-argyriou`.

[42] T. de Graauw et al., *Observing with the ISO Short-Wavelength Spectrometer.*, **315**, L49 (1996).

[43] J. R. Houck et al., *The Infrared Spectrograph (IRS) on the Spitzer Space Telescope*, **154**, 18 (2004).

[44] M. McClure, *Observational 5-20 μm Interstellar Extinction Curves Toward Star-Forming Regions Derived From Spitzer IRS Spectra*, **693**, L81 (2009).

[45] M. L. van Gelder et al., *JOYS+: Mid-infrared detection of gas-phase SO_2 emission in a low-mass protostar. The case of NGC 1333 IRAS 2A: Hot core or accretion shock?*, **682**, A78 (2024).

[46] Ł. Tychoniec et al., *JWST Observations of Young protoStars (JOYS): Linked accretion and ejection in a Class I protobinary system*, arXiv e-prints , arXiv:2402.04343 (2024).

[47] R. Gommers et al., *scipy/scipy: SciPy 1.13.1*, 2024.

[48] M. A. Branch, T. F. Coleman, and Y. Li, *A Subspace, Interior, and Conjugate Gradient Method for Large-Scale Bound-Constrained Minimization Problems*, SIAM Journal on Scientific Computing **21**, 1 (1999).

[49] B. Tabone et al., *A rich hydrocarbon chemistry and high C to O ratio in the inner disk around a very low-mass star*, Nature Astronomy **7**, 805 (2023).

[50] I. E. Gordon et al., *The HITRAN2020 molecular spectroscopic database*, **277**, 107949 (2022).

[51] E. Roueff, H. Abgrall, P. Czachorowski, K. Pachucki, M. Puchalski, and J. Komasa, *The full infrared spectrum of molecular hydrogen*, **630**, A58 (2019).

[52] B. D. Savage and J. S. Mathis, *Observed properties of interstellar dust.*, **17**, 73 (1979).

[53] D. R. Flower, G. Pineau des Forets, and T. W. Hartquist, *Theoretical studies of interstellar molecular shocks - I. General formulation and effects of the ion-molecule chemistry*, Monthly Notices of the Royal Astronomical Society **216**, 775 (1985).

[54] B. Godard, G. Pineau des Forêts, P. Lesaffre, A. Lehmann, A. Gusdorf, and E. Falgarone, *Models of irradiated molecular shocks*, **622**, A100 (2019).

[55] J. S. Mathis, P. G. Mezger, and N. Panagia, *Interstellar radiation field and dust temperatures in the diffuse interstellar medium and in giant molecular clouds*, **128**, 212 (1983).

[56] B. Godard, G. Pineau Des Forêts, and S. Bialy, *Shocks in the Warm Neutral Medium I – Theoretical model*, arXiv e-prints , arXiv:2404.19533 (2024).

[57] J. A. Villa-Vélez, B. Godard, P. Guillard, and G. Pineau des Forêts, *Radiative and mechanical energies in galaxies I. Contributions of molecular shocks and PDRs in 3C 326 N*, arXiv e-prints , arXiv:2405.02058 (2024).

[58] Y.-L. Yang, N. J. E. II, J. D. Green, M. M. Dunham, and J. K. JÃžrgensen, *The Class 0 Protostar BHR71: Herschel Observations and Dust Continuum Models*, The Astrophysical Journal **835**, 259 (2017).

[59] C. L. H. Hull, V. J. M. Le Gouellec, J. M. Girart, J. J. Tobin, and T. L. Bourke, *Understanding the Origin of the Magnetic Field Morphology in the Wide-binary Protostellar System BHR 71*, **892**, 152 (2020).

[60] D. Rosenthal, F. Bertoldi, and S. Drapatz, *ISO-SWS observations of OMC-1: H_2 and fine structure lines*, **356**, 705 (2000).

[61] T. Giannini, B. Nisini, and D. Lorenzetti, *Far-Infrared Investigation of Class 0 Sources: Line Cooling*, **555**, 40 (2001).

[62] D. A. Neufeld, G. J. Melnick, P. Sonnentrucker, E. A. Bergin, J. D. Green, K. H. Kim, D. M. Watson, W. J. Forrest, and J. L. Pipher, *Spitzer Observations of HH 54 and HH 7-11: Mapping the H_2 Ortho-to-Para Ratio in Shocked Molecular Gas*, **649**, 816 (2006).

[63] D. A. Neufeld, B. Nisini, T. Giannini, G. J. Melnick, E. A. Bergin, Y. Yuan, S. Maret, V. Tolls, R. Güsten, and M. J. Kaufman, *Spitzer Spectral Line Mapping of Protostellar Outflows. I. Basic Data and Outflow Energetics*, **706**, 170 (2009).

[64] D. A. Neufeld, C. DeWitt, P. Lesaffre, S. Cabrit, A. Gusdorf, L. N. Tram, and M. Richter, *SOFIA/EXES Observations of Warm H_2 at High Spectral Resolution: Witnessing Para-to-ortho Conversion behind a Molecular Shock Wave in HH7*, **878**, L18 (2019).

[65] R. Bachiller, F. Gueth, S. Guilloteau, M. Tafalla, and A. Dutrey, *The origin of the HH 7-11 outflow*, **362**, L33 (2000).

[66] T. Giannini, B. Nisini, D. Neufeld, Y. Yuan, S. Antoniucci, and A. Gusdorf, *Spitzer Spectral Line Mapping of Protostellar Outflows. III. H_2 Emission in L1448, BHR71, and NGC2071*, **738**, 80 (2011).

[67] C. Gieser et al., *JOYS: Disentangling the warm and cold material in the high-mass IRAS 23385+6053 cluster*, **679**, A108 (2023).

[68] R. Cesaroni et al., *IRAS 23385+6053: an embedded massive cluster in the making*, **627**, A68 (2019).

[69] M. Narang et al., *Discovery of a Collimated Jet from the Low-luminosity Protostar IRAS 16253â2429 in a Quiescent Accretion Phase with the JWST*, **962**, L16 (2024).

[70] B. Nisini et al., *PROJECT-J: JWST Observations of HH46 IRS and Its Outflow. Overview and First Results*, **967**, 168 (2024).

[71] K. M. Pontoppidan, N. Evans, J. Bergner, and Y.-L. Yang, *A Constrained Dust Opacity for Models of Dense Clouds and Protostellar Envelopes*, Research Notes of the American Astronomical Society **8**, 68 (2024).

[72] M. G. Burton, D. J. Hollenbach, and A. G. G. Tielens, *Mid-Infrared Rotational Line Emission from Interstellar Molecular Hydrogen*, **399**, 563 (1992).

[73] J. Erkal, B. Nisini, D. Coffey, F. Bacciotti, P. Hartigan, S. Antoniucci, T. Giannini, J. Eislöffel, and C. F. Manara, *Probing Jets from Young Embedded Sources: Clues from HST Near-IR [Fe II] Images*, **919**, 23 (2021).

Appendices

Appendix A

Line fits of every aperture

A.1 Aperture A

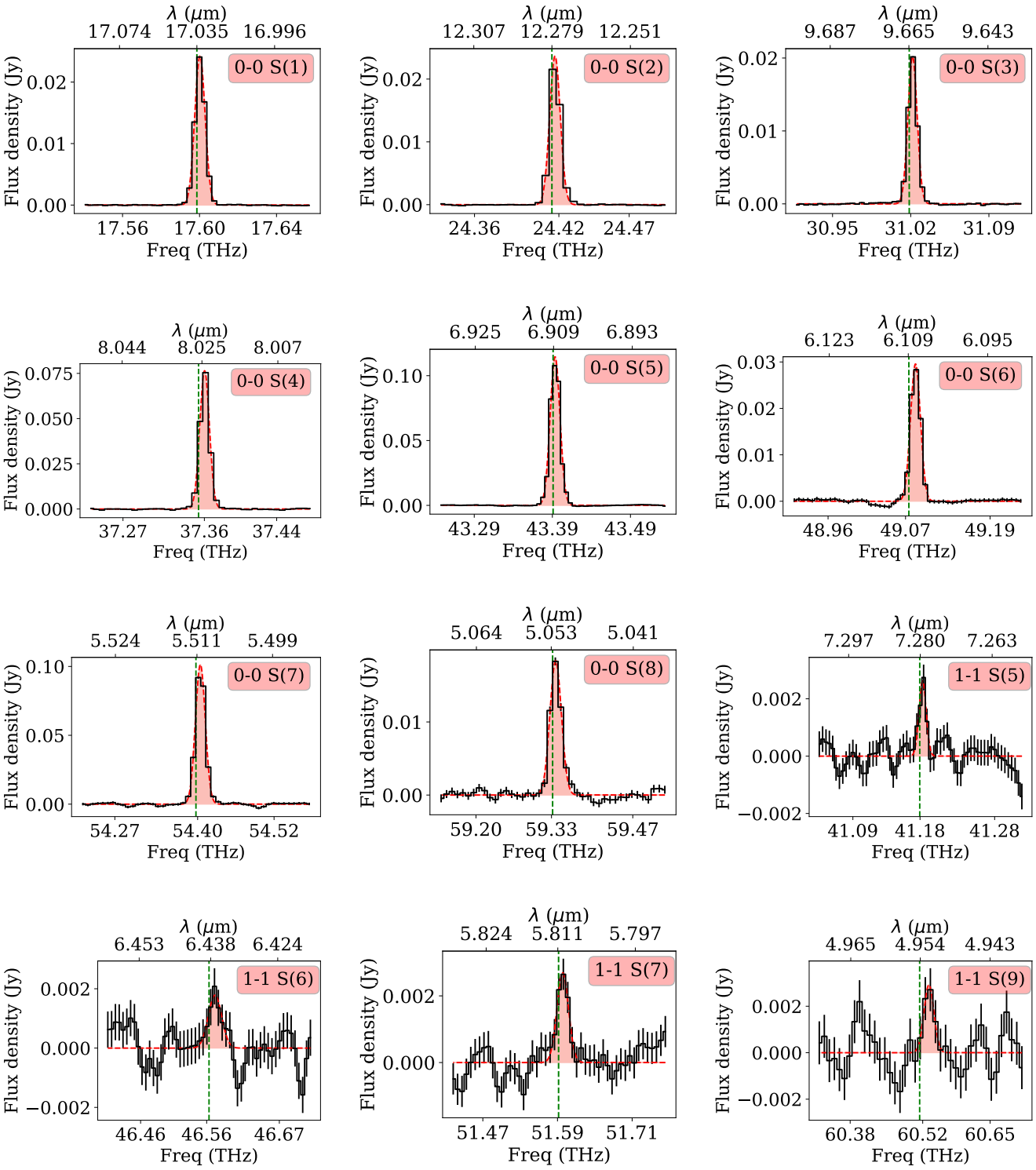

Figure A.1: *The Gaussian line fit of every molecular hydrogen transition detected in aperture A. The black line is the data, the red line is the fit. The shaded area indicates the integrated flux. The green dotted line shows the rest wavelength of the line.*

Version of June 14, 2024– Created June 14, 2024 - 14:55

A.2 Aperture B

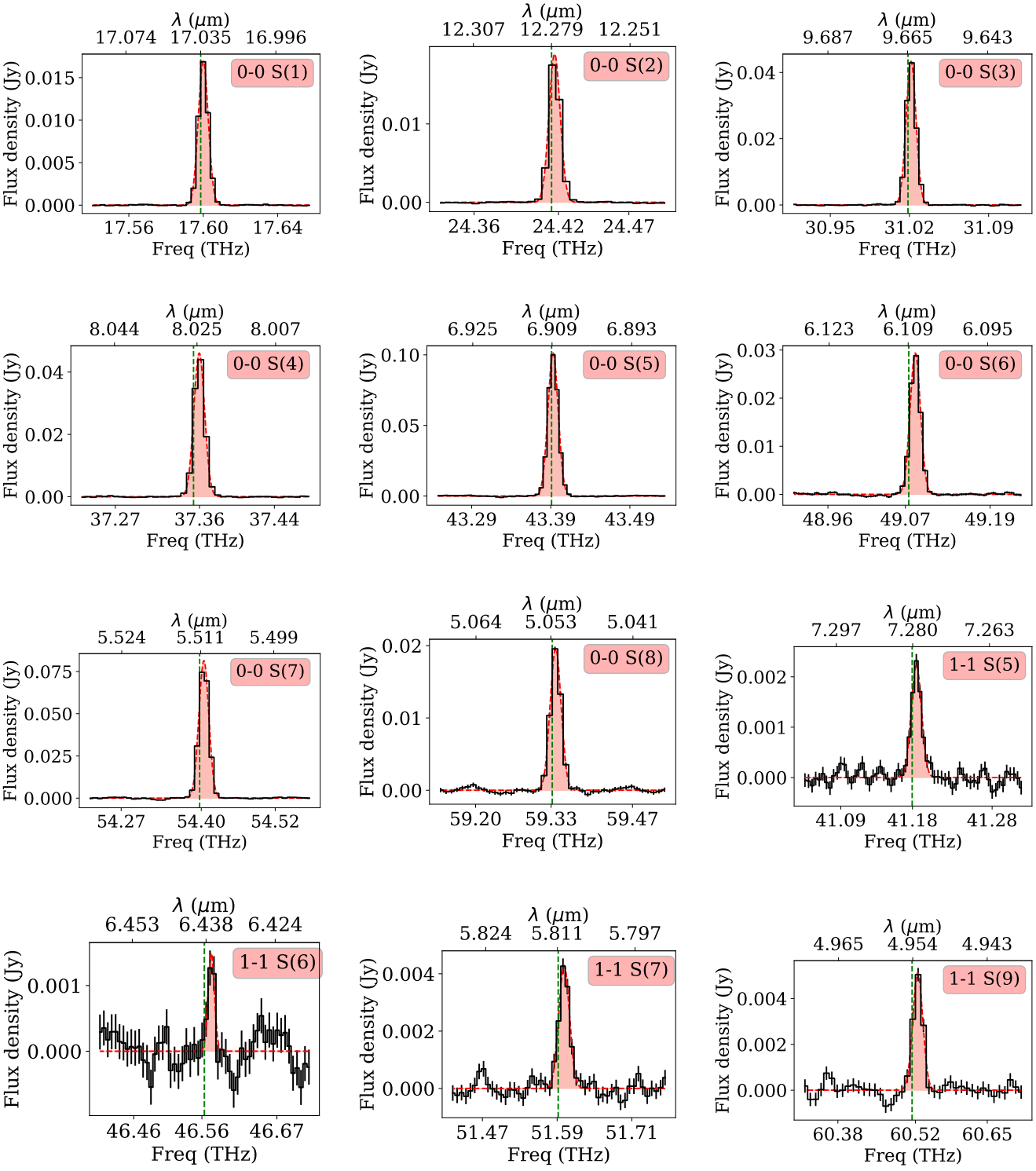

Figure A.2: *Same as Figure A.1 but for aperture B*

Version of June 14, 2024– Created June 14, 2024 - 14:55

A.3 Aperture C

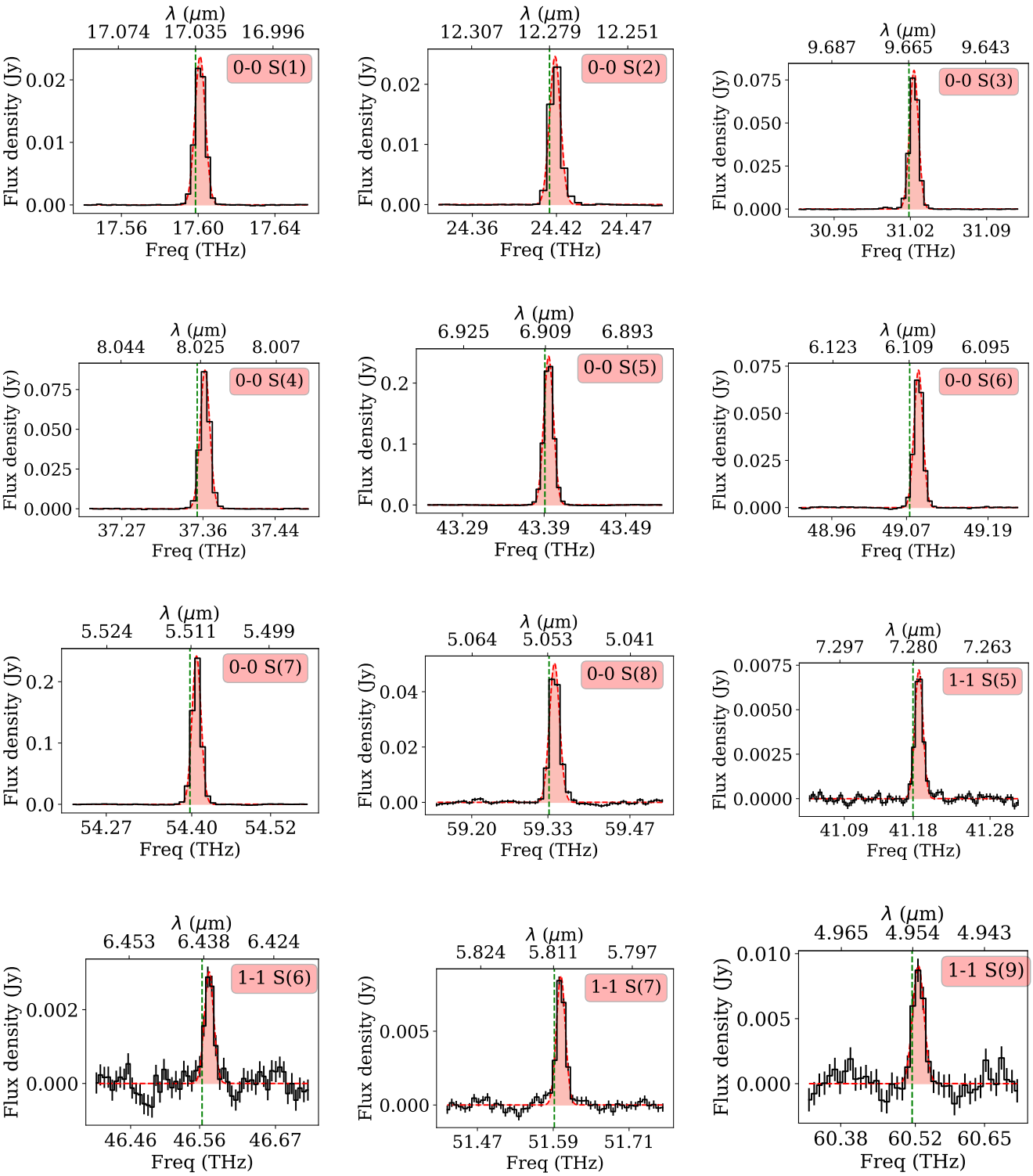

Figure A.3: *Same as Figure A.1 but for aperture C*

Version of June 14, 2024– Created June 14, 2024 - 14:55

A.4 Aperture D

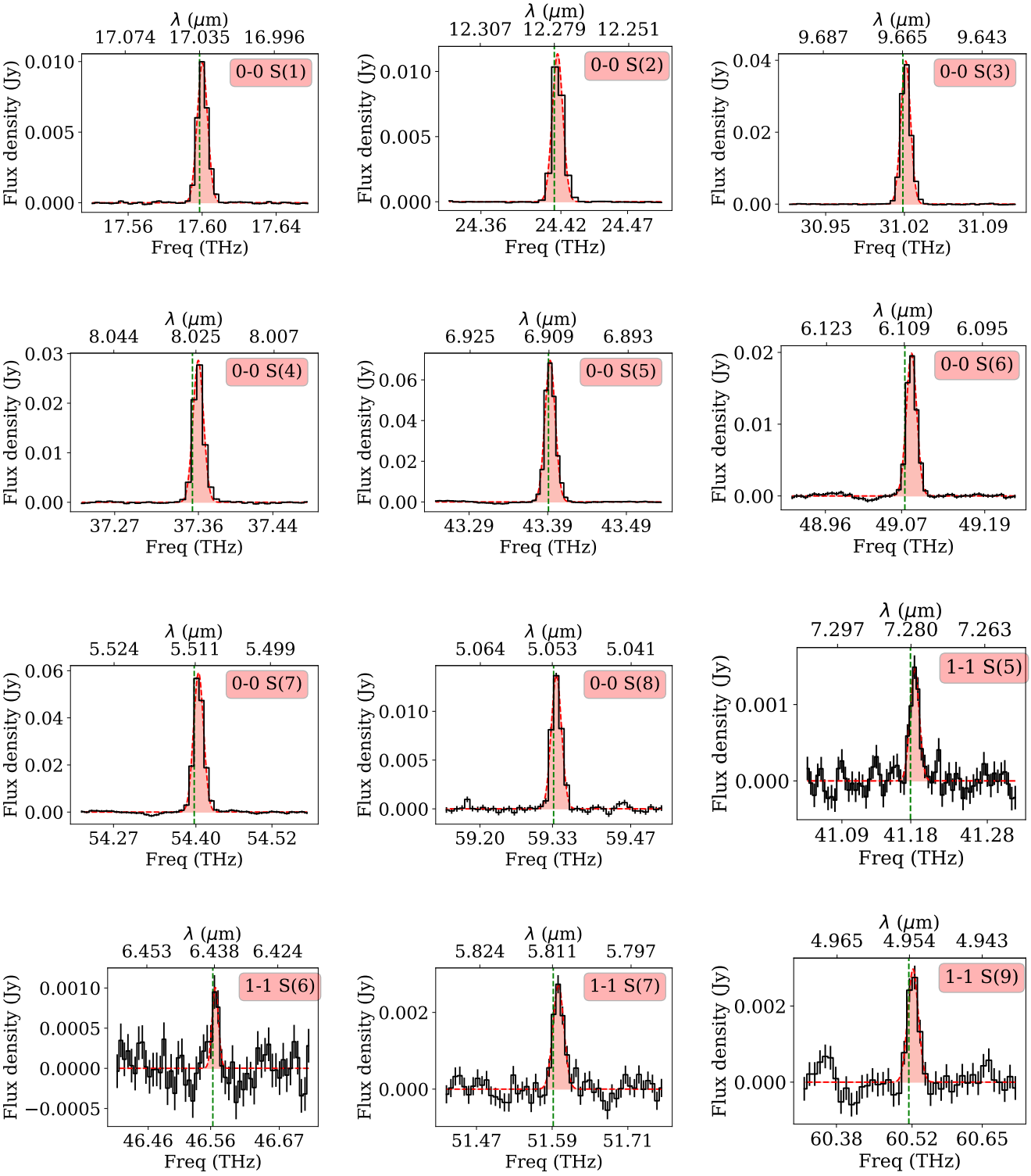

Figure A.4: *Same as Figure A.1 but for aperture D*

Version of June 14, 2024– Created June 14, 2024 - 14:55

A.5 Aperture E

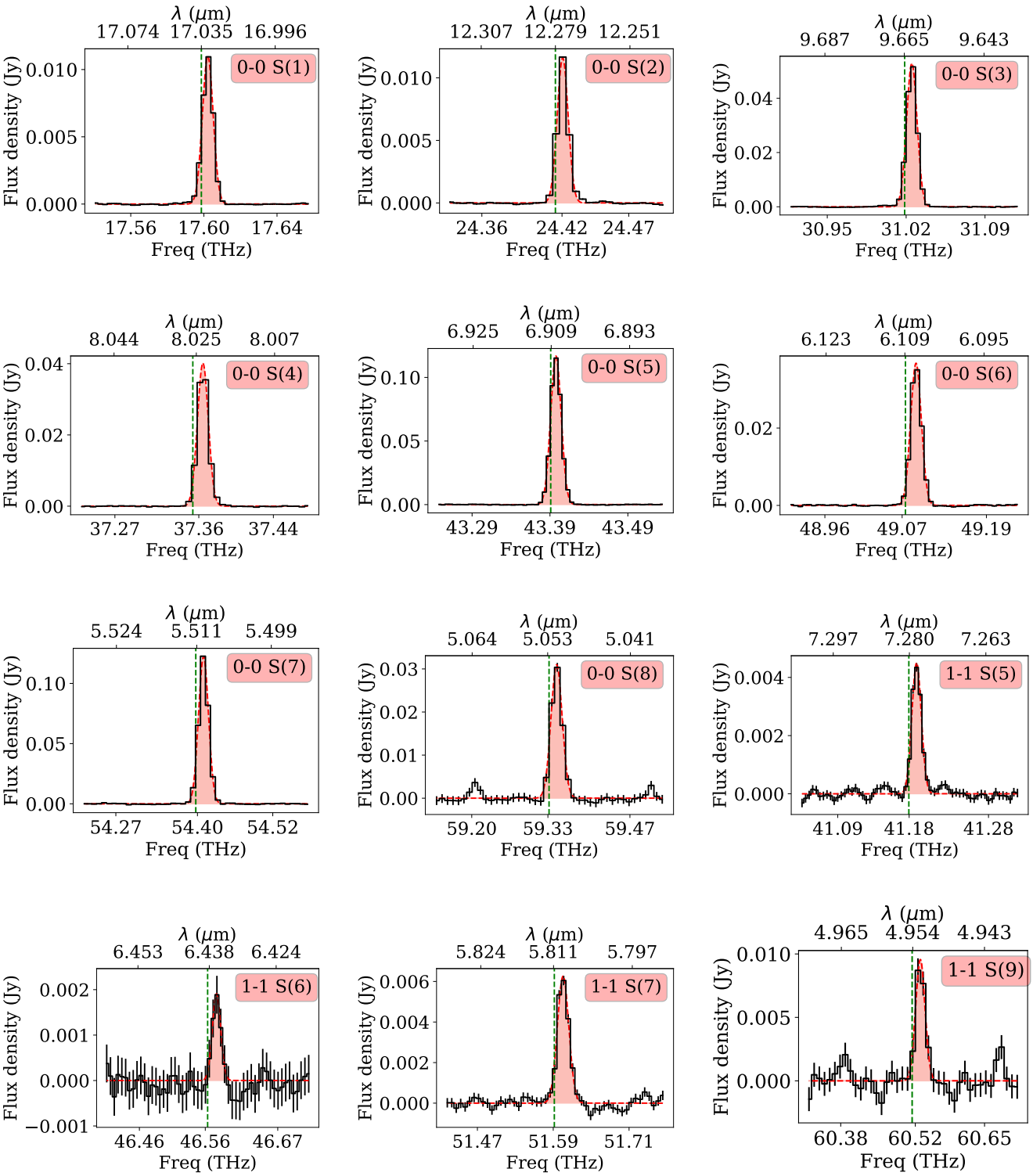

Figure A.5: *Same as Figure A.1 but for aperture E*

Version of June 14, 2024– Created June 14, 2024 - 14:55

A.6 Aperture F

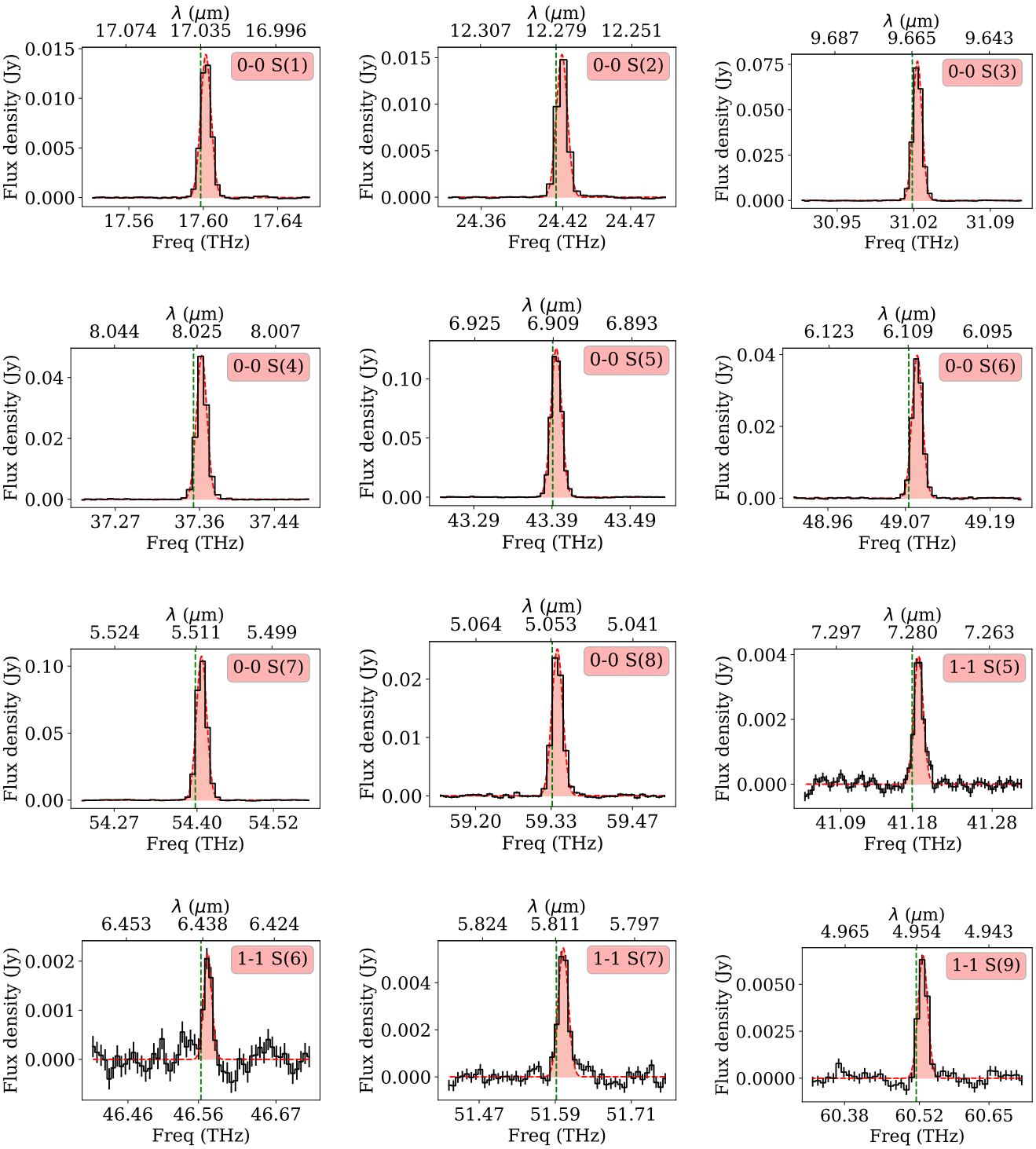

Figure A.6: *Same as Figure A.1 but for aperture F*

Version of June 14, 2024– Created June 14, 2024 - 14:55

Appendix B

Fluxes of H2 lines

Table B.1: *Integrated flux of all molecular hydrogen transitions detected, corresponding to the shaded area of the line plots in Appendix A.*

Line	Wavelength	Region A	Region B	Region C
0-0 S1	17.035	1.62(-15)±4.68(-18)	1.14-15±4.27(-18)	6.94(-16)±5.48(-18)
0-0 S2	12.279	2.23(-15)±8.95(-18)	1.88-15±1.05(-17)	1.13(-15)±4.97(-18)
0-0 S3	9.6649	2.08(-15)±1.27(-17)	4.73-15±1.62(-17)	4.30(-15)±1.28(-17)
0-0 S4	8.0258	1.02(-14)±7.01(-17)	6.64-15±3.23(-17)	4.05(-15)±2.64(-17)
0-0 S5	6.9091	1.80(-14)±7.90(-17)	1.64-14±5.58(-17)	1.14(-14)±5.71(-17)
0-0 S6	6.1089	5.22(-15)±8.24(-17)	5.39-15±6.48(-17)	3.74(-15)±5.72(-17)
0-0 S7	5.51116	1.96(-14)±2.84(-16)	1.64-14±1.10(-16)	1.17(-14)±1.02(-16)
0-0 S8	5.0528	4.64(-15)±2.38(-16)	4.61-15±8.99(-17)	3.12(-15)±7.88(-17)
1-1 S5	7.2801191	3.02(-16)±9.36(-17)	3.50-16±2.92(-17)	2.48(-16)±3.19(-17)
1-1 S6	6.4383478	4.53(-16)±1.75(-16)	1.80-16±5.94(-17)	1.27(-16)±4.39(-17)
1-1 S7	5.8108616	4.91(-16)±1.39(-16)	9.28-16±6.90(-17)	5.91(-16)±6.84(-17)
1-1 S9	4.9540951	7.04(-16)±3.03(-16)	1.21-15±1.03(-16)	6.97(-16)±9.67(-17)

Line	Wavelength	Region D	Region E	Region F
0-0 S1	17.035	1.62(-15)±4.10(-18)	8.12(-16)±3.58(-18)	1.01(-15)±5.98(-18)
0-0 S2	12.279	2.41(-15)±8.82(-18)	1.19(-15)±9.16(-18)	1.56(-15)±1.20(-17)
0-0 S3	9.6649	8.19(-15)±2.98(-17)	6.16(-15)±2.15(-17)	8.12(-15)±1.88(-17)
0-0 S4	8.0258	1.17(-14)±3.48(-17)	5.87(-15)±2.20(-17)	6.61(-15)±2.82(-17)
0-0 S5	6.9091	3.60(-14)±5.08(-17)	1.98(-14)±3.78(-17)	2.14(-14)±4.57(-17)
0-0 S6	6.1089	1.19(-14)±6.27(-17)	7.04(-15)±5.80(-17)	7.33(-15)±5.31(-17)
0-0 S7	5.51116	4.16(-14)±1.09(-16)	2.43(-14)±1.03(-16)	2.17(-14)±7.86(-17)
0-0 S8	5.0528	1.09(-14)±1.93(-16)	7.45(-15)±3.09(-16)	5.95(-15)±8.26(-17)
1-1 S5	7.2801191	9.65(-16)±3.44(-17)	6.98(-16)±2.89(-17)	5.76(-16)±2.93(-17)
1-1 S6	6.4383478	5.12(-16)±6.27(-17)	3.49(-16)±4.42(-17)	3.13(-16)±4.55(-17)
1-1 S7	5.8108616	1.55(-15)±6.63(-17)	1.46(-15)±6.37(-17)	1.10(-15)±5.51(-17)
1-1 S9	4.9540951	2.34(-15)±2.87(-16)	2.11(-15)±2.99(-16)	1.45(-15)±1.06(-16)

Notes: The brackets indicate the order of magnitude: $b(a)$ is $b \times 10^a$.

Appendix C

Limitations of the shock model

A short summary of the assumptions and simulation conditions of the shock code used by K23. For a complete overview, we refer to the paper, in which it is discussed extensively.

Geometry	**Magnetic Field Orientation**	**Self-irradiation**
The model treats a plane-parallel shock front, thus ignoring geometry. This may overestimate the post-shock density, particularly for J-type shocks.	The magnetic field orientation is assumed to be perpendicular to the shock. If this is not the case, compression can lead to a change in field geometry.	Shocks in which H_2 is dissociated are self-irradiated. These shocks are not simulated, which limits the J-type shock to v_s <30km s^{-1}.
Stationary shocks	**Grain chemistry**	**Course grid**
The model only simulates stationary shocks, which implies that the stationary structure has enough time to develop fully.	Grain-grain interaction is omitted, which is only likely a valid assumption for v_s <25km s^{-1} and $n_H < 10^5$cm^{-3}	The grid is extensive, but therefore relatively course. This makes the constrain on the conditions still broad.

Appendix D

Intensities of all models

The figure for aperture D is shown in the Results section.

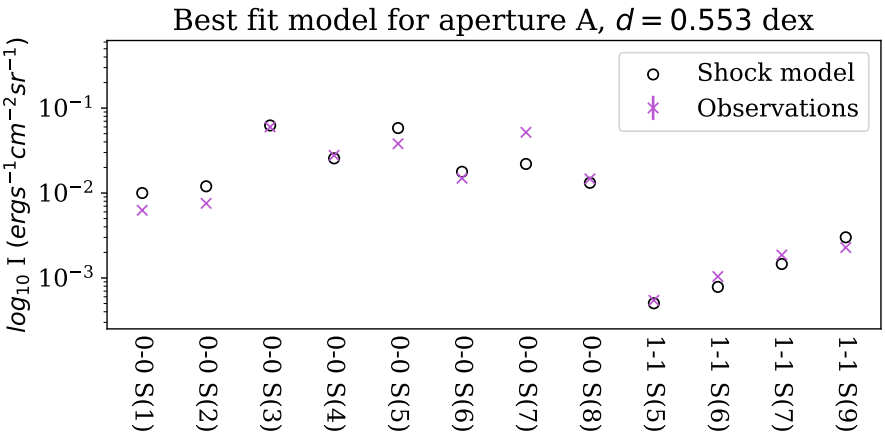

Figure D.1: *The best-fit model for aperture A using the minimum distance defined in Section 2.3. The minimum distance is 0.553 dex. The intensities are plotted on a logarithmic axis, and the best-fit model is shown as open black circles. The uncertainty on the intensity is very small, which is amplified by the log scale and the fact that the intensities are corrected for extinction. The x-axis shows the transitions associated with the intensities.*

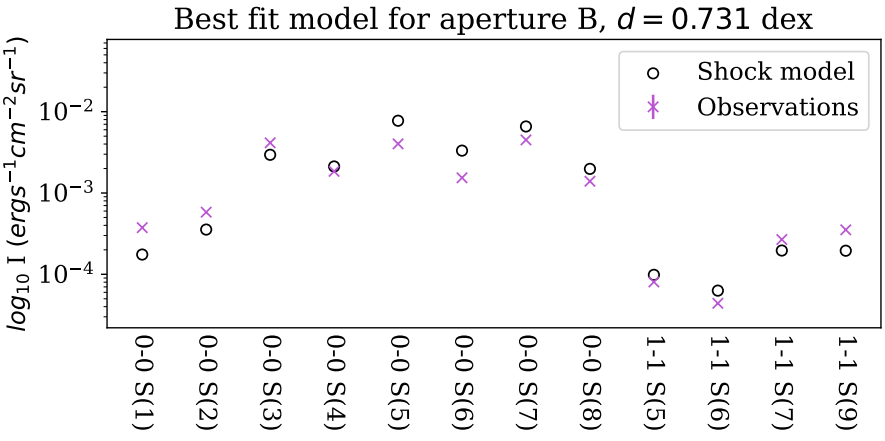

Figure D.2: *Same as Figure D.1 but for aperture B, which has a minimum distance of 0.731 dex.*

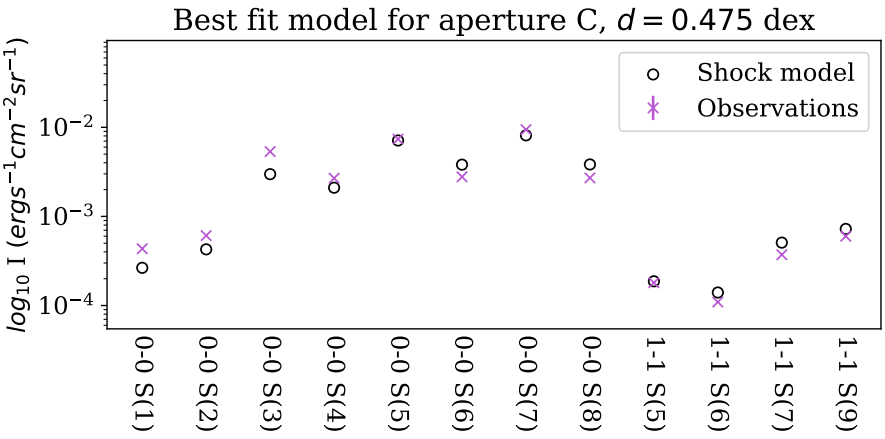

Figure D.3: *Same as Figure D.1 but for aperture C, which has a minimum distance of 0.475 dex.*

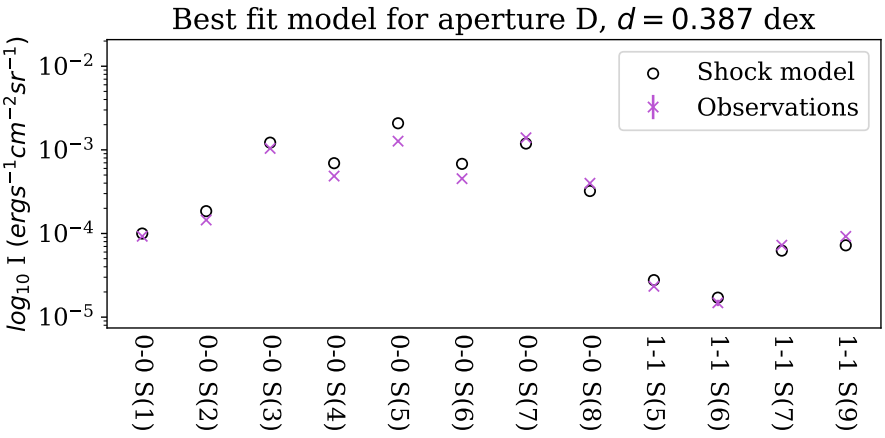

Figure D.4: *Same as Figure D.1 but for aperture D, which has a minimum distance of 0.387 dex.*

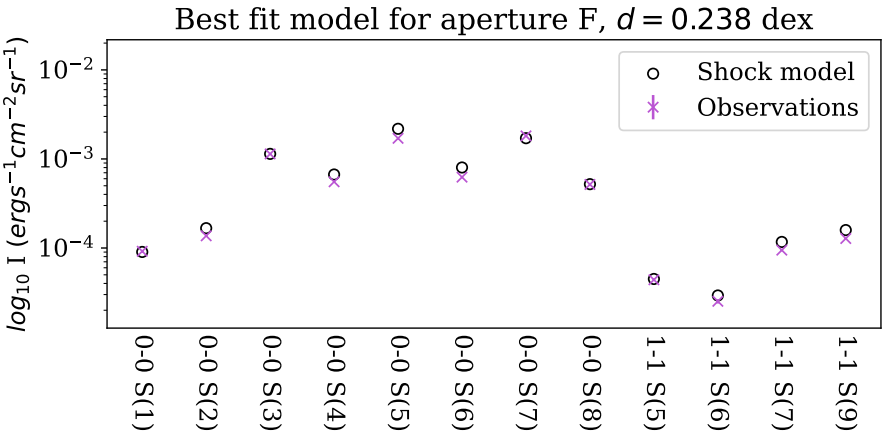

Figure D.5: *Same as Figure D.1 but for aperture F, which has a minimum distance of 0.238 dex.*

Version of June 14, 2024– Created June 14, 2024 - 14:55

Appendix E

Full report model comparison

Aperture	$nH^{(a)}$ (cm^{-2})	Vs (km s^{-1})	b$^{(b)}$	G0$^{(c)}$	$\zeta^{(d)}$	X(PAH)
A	10^8	90.0	10.0	100.0	10^{-15}	10^{-7}
	10^8	80.0	10.0	1000.0	$10^{-15}/10^{-16}$	10^{-6}
	10^8	60.0	3.0	0.1	$10^{-15}/10^{-16}$	10^{-8}
	10^8	60.0	3.0	0	$10^{-15}/10^{-17}$	10^{-8}
	10^8	50.0	3.0	0.1	$10^{-16}/10^{-17}$	$10^{-7}/10^{-8}$
	10^8	50.0	3.0	0.1	$10^{-16}/10^{-17}$	10^{-6}
	10^8	50.0	3.0	1.0	$10^{-15}/10^{-16}$	10^{-6}
	10^7	90.0	10.0	0.1	10^{-17}	10^{-6}
	10^7	60.0	3.0	0.1	10^{-16}	10^{-6}
	10^7	50.0	3.0	1.0	$10^{-15}/10^{-17}$	10^{-6}
B	10^4	50.0	3.0	10.0	10^{-15}	10^{-7}
	10^7	60.0	3.0	1000.0	10^{-16}	10^{-6}
	10^7	50.0	3.0	1000.0	10^{-16}	10^{-6}
C	10^5	30.0	3.0	100.0	$10^{-15}/10^{-17}$	10^{-6}
	10^4	80.0	10.0	10.0	$10^{-15}/10^{-17}$	10^{-7}
	10^4	80.0	10.0	1.0	10^{-15}	10^{-6}
	10^4	60.0	3.0	1.0	10^{-15}	10^{-8}
	10^4	60.0	3.0	0	10^{-15}	10^{-6}
	10^4	50.0	3.0	10.0	10^{-17}	10^{-6}
D	10^3	60.0	3.0	10.0	$10^{-15}/10^{-17}$	10^{-7}
	10^3	80.0	10.0	10.0	10^{-15}	10^{-6}
E	10^4	50.0	3.0	100.0	10^{-17}	10^{-7}
	10^4	40.0	3.0	100.0	10^{-17}	10^{-6}
	10^3	90.0	10.0	10.0	$10^{-15}/10^{-17}$	10^{-6}
F	10^3	90.0	10.0	10.0	$10^{-15}/10^{-17}$	10^{-6}

Table E.1: *All best-fit models for the observed intensities in the outflow positions of BHR71 IRS1. The best-fit models were calculated for different values of A_K, extinction correction, within the uncertainty of A_K. If only one of the initial parameters differed for two models, they were combined in the Table.*

Appendix F

Grids of all models

In K23, they provide a grid in the 4D parameter space, where they keep ζ_{H_2} and X(PAH) fixed to show the resulting shock types for certain initial conditions. We recreated this grid to show in which regions of 4D space the minima in the distance between the model and the observations are. This was done only for intensities corrected using the derived A_K, not for all A_K within the uncertainty. The colour in the grid is based on the value in the grid, which is the distance in units of (dex) given by equation 2.16. Higher distances are purple while lower distances (better models) are yellow, with green as a transition colour. The colours are capped at the median distance, to visualise where the better models are. The grid can be used to reduce the parameter space in order to simulate shock models using finer initial conditions. The grids for the apertures B-F are provided in this appendix, the grid for aperture A can be found in the discussion, Section 4.5. The grids are mostly consistent with the ranges of values found for the initial conditions within the extinction uncertainty. Important to note is that the grid does not distinguish between physical and unphysical models at this point. Low minimum distance models may have $T_{max} < T_{hot}$.

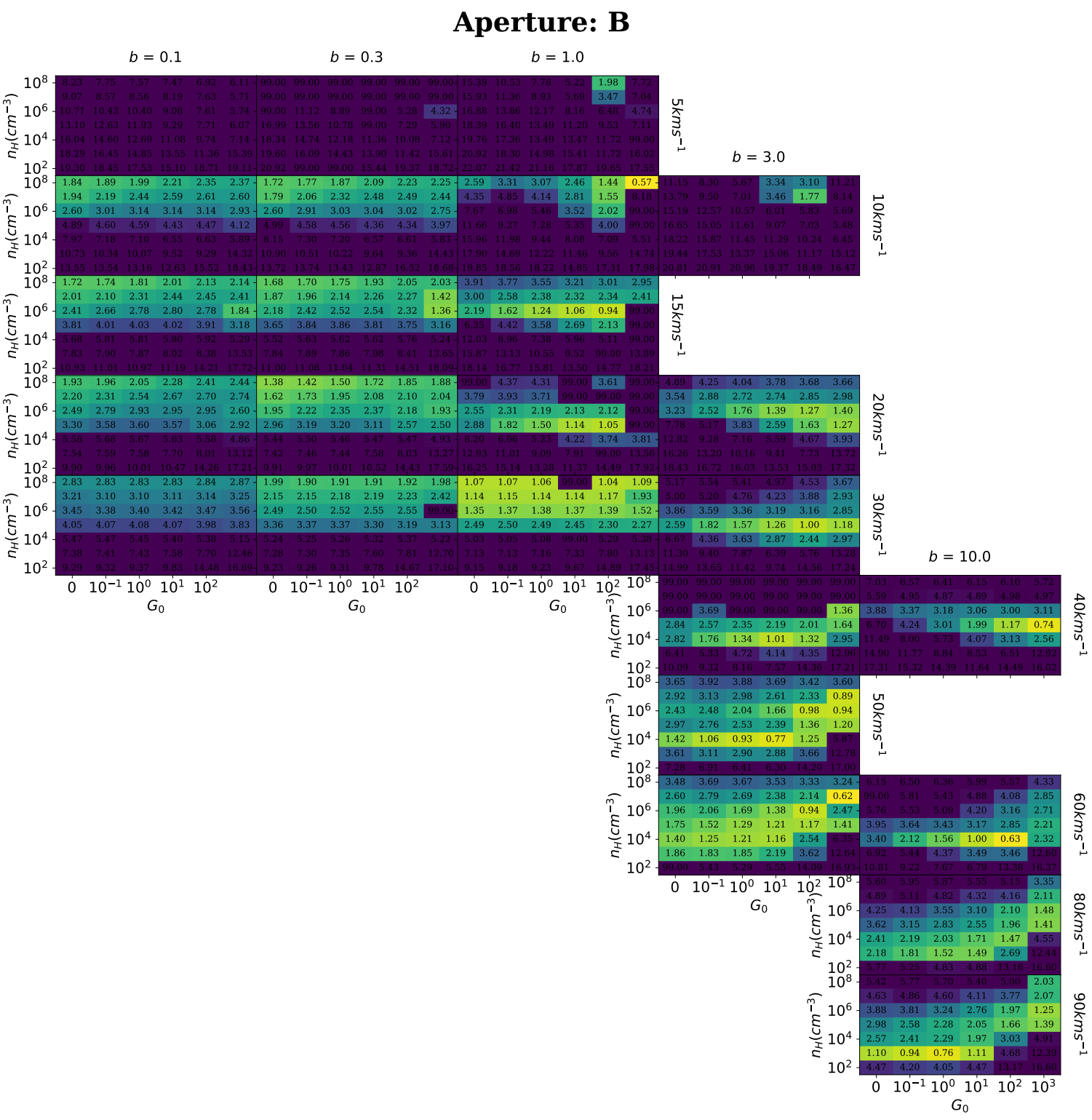

Figure F.1: *4D grid of Aperture B with distances between models and the observation. ζ_{H_2} and $X(PAH)$ are set to their best-fit model values, which for Aperture A are $\zeta_{H_2} = 10^{-17}$ and $X(PAH) = 10^{-6}$. The colour is based on the value in the grid, which is the distance in units of (dex) given by equation 2.16. Higher distances are purple while lower distances (better models) are yellow, with green as a transition colour. The colours are capped at the median distance, to visualise where the better models are. The best value here is inconsistent with the conditions reported, due to the fact that the best-fit model in the grid has $T_{max} < T_{hot}$.*

Version of June 14, 2024– Created June 14, 2024 - 14:55

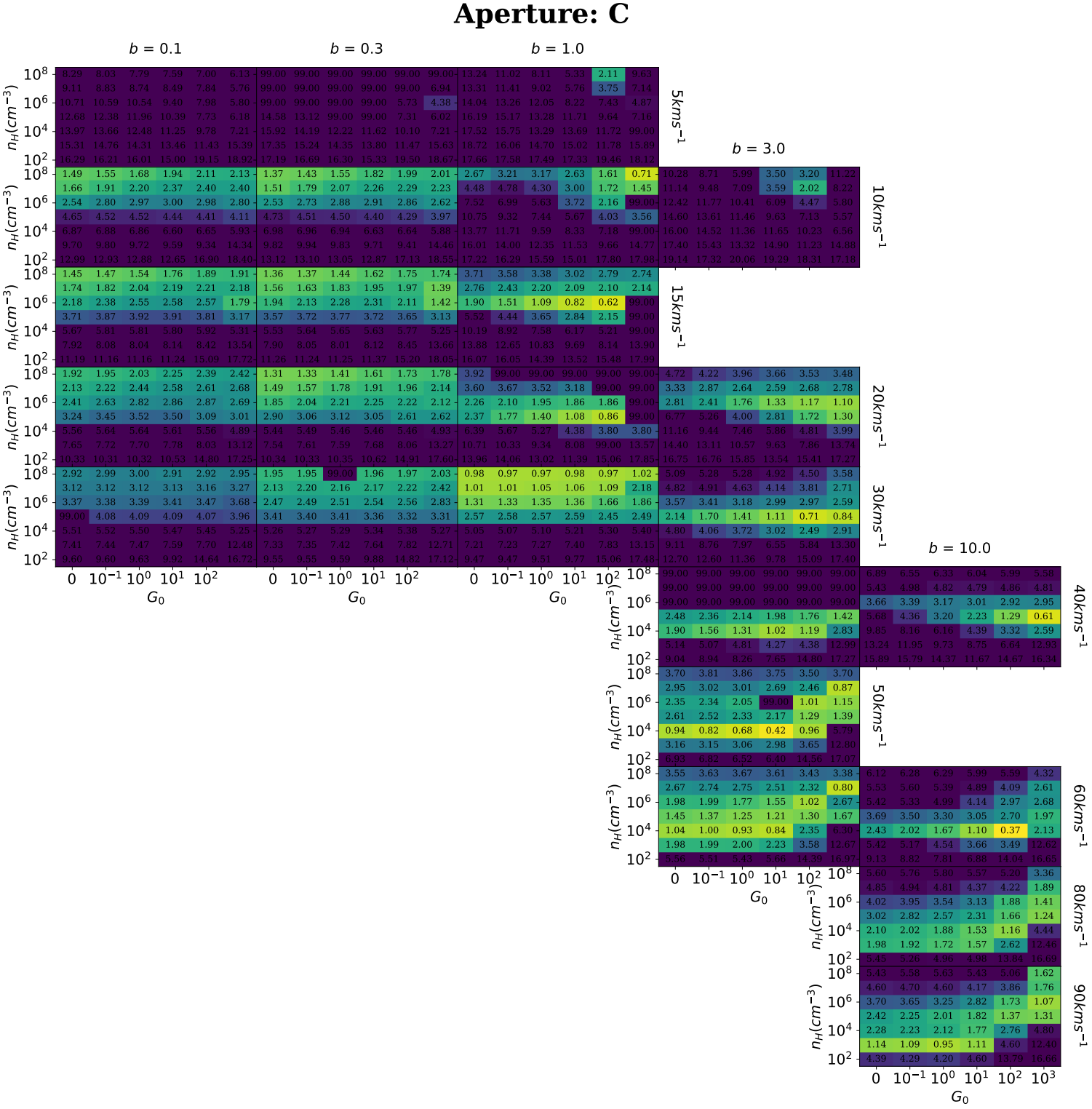

Figure F.2: *Same as Figure F.1 but for aperture C.*

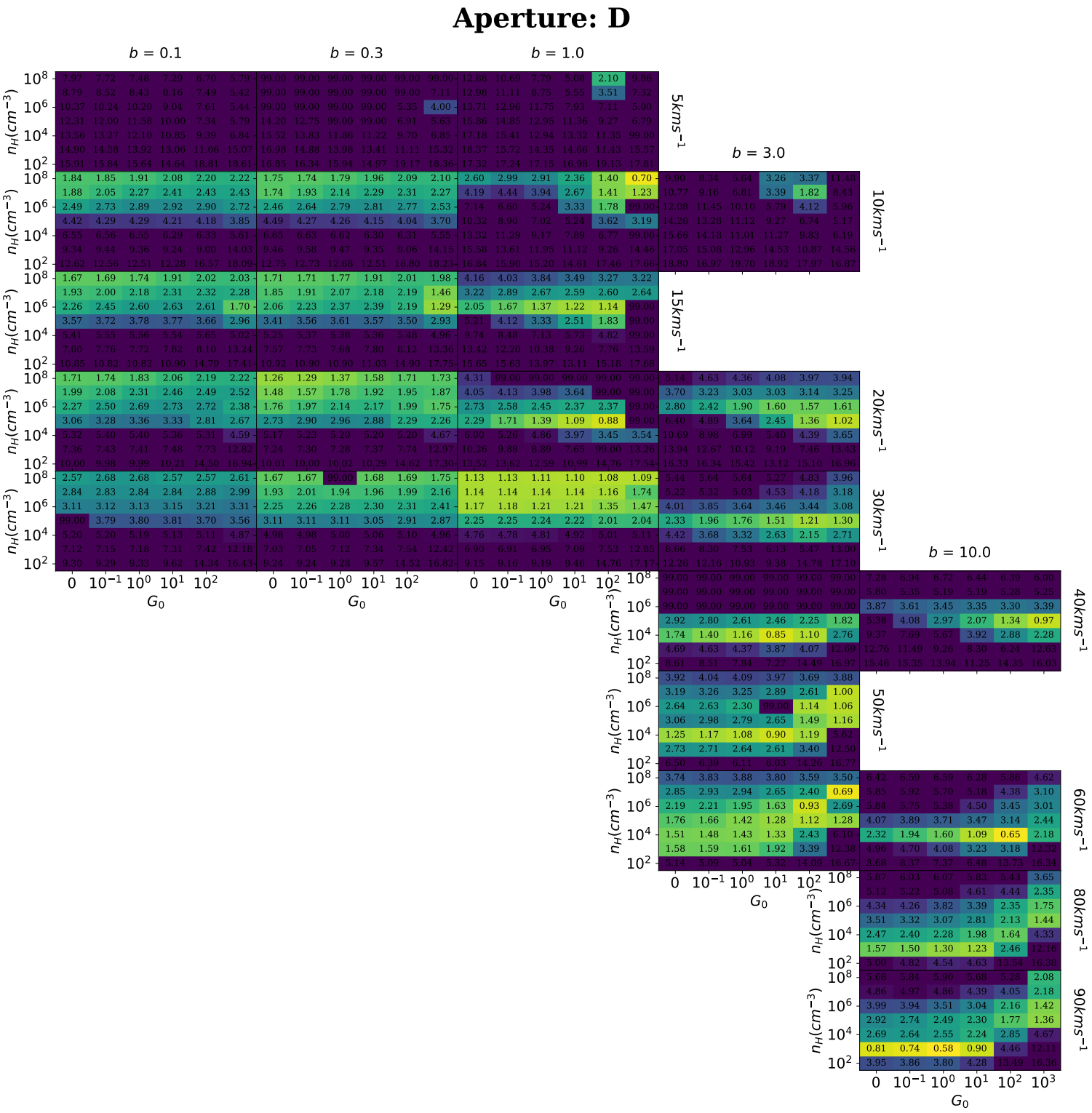

Figure F.3: *Same as Figure F.1 but for aperture D.*

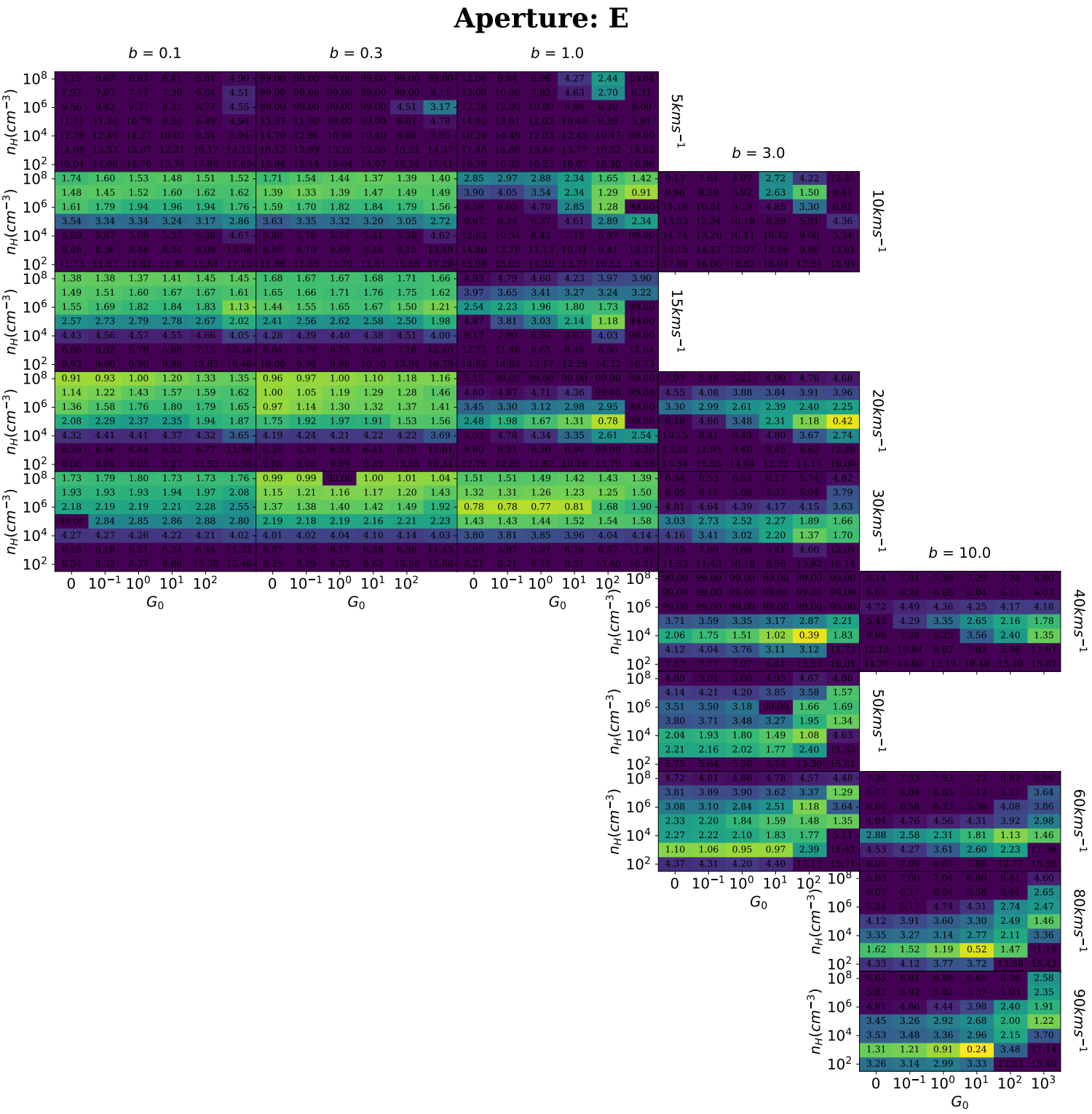

Figure F.4: *Same as Figure F.1 but for aperture E.*

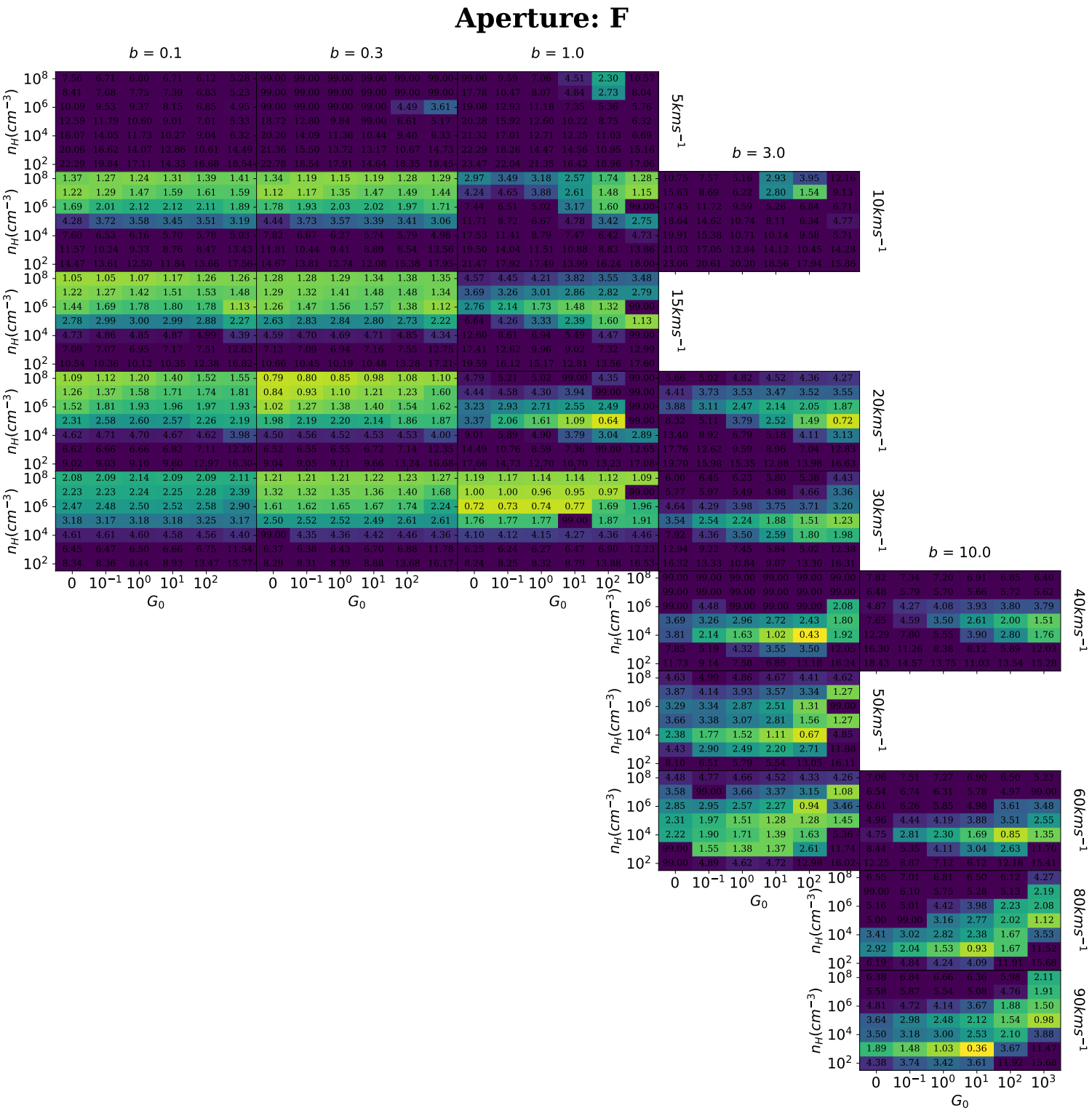

Figure F.5: *Same as Figure F.1 but for aperture F.*

Version of June 14, 2024– Created June 14, 2024 - 14:55